Chemical proteomics reveals soluble epoxide hydrolase as a therapeutic target for ocular neovascularization

Rania S. Sulaiman,[†,‡,⊥] Bomina Park,[†,‡] Sardar Pasha Sheik Pran Babu,[†] Yubing Si,[§] Rakshin Kharwadkar,[§] Sayak K. Mitter,[†,&] Bit Lee,[#] Wei Sun,[#] Xiaoping Qi, [†,&] Michael E. Boulton,[†,&] Samy Meroueh,[§,||] Xiang Fei,[#] Seung-Yong Seo,[*,#] Timothy W. Corson[*,†,‡,§,||]

[†]Eugene and Marilyn Glick Eye Institute, Department of Ophthalmology, [‡]Department of Pharmacology and Toxicology, [§]Department of Biochemistry and Molecular Biology, [||]Melvin and Bren Simon Cancer Center, Indiana University School of Medicine, Indianapolis, Indiana, United States of America. [⊥]Department of Biochemistry, Faculty of Pharmacy, Cairo University, Cairo, Egypt. [#]College of Pharmacy, Gachon University, Incheon, South Korea. [&]Department of Ophthalmology, University of Alabama Birmingham, Birmingham, Alabama, United States of America

*Corresponding authors. E-mail: tcorson@iu.edu, Phone: +1–317–274–3305

Address: 1160 West Michigan Street, Indianapolis, IN 46202 USA

E-mail: syseo@gachon.ac.kr, Phone: +82-32-820-4949

Address: 191 Hambakoero, Yeonsu-gu, Incheon, Korea 21936

This is the author's manuscript of the article published in final edited form as:
Sulaiman, R. S., Park, B., Sheik Pran Babu, S. P., Si, Y., Kharwadkar, R., Mitter, S. K., ... & Meroueh, S. O. (2017). Chemical Proteomics Reveals Soluble Epoxide Hydrolase as a Therapeutic Target for Ocular Neovascularization. ACS chemical biology, 13(1), 45-52. http://dx.doi.org/10.1021/acschembio.7b00854

ABSTRACT

The standard-of-care therapeutics for the treatment of ocular neovascular diseases like wet age-related macular degeneration (AMD) are biologics targeting vascular endothelial growth factor signaling. There are currently no FDA approved small molecules for treating these blinding eye diseases. Therefore, therapeutic agents with novel mechanisms are critical to complement or combine with existing approaches. Here, we identified soluble epoxide hydrolase (sEH), a key enzyme for epoxy fatty acid metabolism, as a target of an antiangiogenic homoisoflavonoid, SH-11037. SH-11037 inhibits sEH *in vitro* and *in vivo* and docks to the substrate binding cleft in the sEH hydrolase domain. sEH levels and activity are upregulated in the eyes of a choroidal neovascularization (CNV) mouse model. sEH is overexpressed in human wet AMD eyes, suggesting that sEH is relevant to neovascularization. Known sEH inhibitors delivered intraocularly suppressed CNV. Thus, by dissecting a bioactive compound's mechanism, we identified a new chemotype for sEH inhibition and characterized sEH as a target for blocking the CNV that underlies wet AMD.

Ocular neovascularization is the underlying cause of blindness in diseases such as retinopathy of prematurity (ROP), proliferative diabetic retinopathy (PDR), and wet age-related macular degeneration (AMD), which cause blindness in infants, adults of working age and the elderly, respectively.[1] Current FDA approved treatments for wet AMD focus on inhibiting the vascular endothelial growth factor (VEGF) signaling pathway using biologics such as ranibizumab and aflibercept.[2] Despite the success of these therapeutic agents, their association with ocular and systemic side effects due to inhibition of such a major angiogenic pathway, and the presence of resistant and refractory patient populations complicate their use.[3, 4] Thus, discovery of new therapeutic targets is crucial. Alternative angiogenic targets could lead to new therapeutics to complement and combine with the existing medications.

We previously characterized a novel antiangiogenic homoisoflavonoid derivative, SH-11037 (**1**; Figure 1a), *in vitro*[5] and *in vivo*.[6] SH-11037 had potent antiangiogenic activities in the laser-induced choroidal neovascularization (L-CNV) mouse model, a widely-used system that recapitulates some of the features of wet AMD.[7] Therefore, characterization of its mechanism of action is important. We used an unbiased forward chemical genetics approach to identify SH-11037 protein targets that might be potentially druggable angiogenic mediators. We first synthesized two photoaffinity reagents **2** and **3** that retained antiangiogenic activity, and a control compound **4** (Figure 1a).[8] The ester group in **2** (shared with SH-11037) was replaced by an amide in **3** for increased stability. The SH-11037-based affinity reagents **2** and **3** were immobilized and used to pull down protein binding partners from a porcine brain lysate. Affinity reagent **3** but not the negative control reagent **4** pulled down a specific protein target, which was identified as soluble epoxide hydrolase (Figure 1b; Supplementary Figure 1). Immunoblot confirmed the identity of the pulled down protein (Figure 1c).

Docking of SH-11037 to sEH (Figure 1d) shows a binding mode in which the compound occupies nearly the entire active site of the enzyme. The homoisoflavonoid group of SH-11037 occupies the site where the catalytic Asp335 and Tyr466 residues of sEH are located.[9] Both aromatic rings of the homoisoflavonoid group are involved in π-π interactions with sEH residues that include His524 and Trp336 (Figure 1e). The benzyl substituent of the peptidic moiety of SH-11037 is ensconced into a hydrophobic cavity created by Trp473, Met503, Ile363, and Phe362. The substituent is located near an opening through which the linker of **2** or **3** is attached to SH-11037. Extensive molecular dynamics simulations reveal that this moiety is flexible as illustrated by root-mean-square deviations for SH-11037 that range from 1.2 to 2.8 Å (Supplementary Figure 2). Animation of the molecular dynamics simulations (Supplementary movie) reveals that the benzene ring periodically adopts a conformation whereby the *para* position of the ring is exposed to solvent. This is likely the conformation that is adopted by the benzyl group in compounds **2** and **3**.

Soluble epoxide hydrolase (sEH, encoded by *EPHX2*) is a 62 kDa bifunctional enzyme that has N-terminal lipid phosphatase (EC 3.1.3.76) and C-terminal epoxide hydrolase (EC 3.3.2.10) activities.[10] While the physiological role of the lipid phosphatase activity of sEH is not fully understood, its epoxide hydrolase activity has been extensively studied due to its role in the metabolism of arachidonic acids' epoxide derivatives, epoxyeicosatrienoic acids (EETs).[11] EETs have proangiogenic effects resulting in accelerating tumor growth,[12] and play a role in hypertension, pain and inflammation. Therefore, sEH inhibitors have been in clinical trials for treating related conditions.[13, 14] But additionally, sEH is involved in the metabolism of the epoxides of ω-3 fatty acids, docosahexaenoic acid (DHA) and eicosapentaenoic acid (EPA), which are more abundant in the eye than EETs.[15]

Following the identification of sEH as a binding target of SH-11037, we tested whether the compound interferes with the epoxide hydrolase activity of sEH *in vitro*, compared to known sEH inhibitors. *Trans*-4-(4-[3-adamantan-1-yl-ureido]-cyclohexyloxy)-benzoic acid (*t*-AUCB (**5**); Figure 2a) is a specific inhibitor of the epoxide hydrolase activity of sEH, widely used in preclinical studies.[16] Meanwhile, 7-(trifluoromethyl)-*N*-(4-(trifluoromethyl)phenyl) benzo[*d*]isoxazol-3-amine (**7**), is a structurally distinct benzisoxazole inhibitor with excellent potency and pharmacokinetic properties.[17] Interestingly, SH-11037 inhibited sEH enzymatic activity *in vitro* in a concentration-dependent manner (Figure 2a), although not as potently as *t*-AUCB or **7**. To test whether these effects are specific to SH-11037, we used as a negative control SH-11098 (**6**), which is a homoisoflavonoid that was found to be inactive in angiogenesis assays *in vitro*.[5] This related compound had minimal inhibitory activity, suggesting that structural features of SH-11037 specifically interact with sEH.

Enzyme kinetics analysis showed that increasing concentrations of SH-11037 decreased V_{max} and increased K_M, revealing that SH-11037 is a mixed-type inhibitor of sEH (Figure 2b, c, d), with $K_i = 1.73 \pm 0.45$ μM. Compound **7** is also a mixed-type inhibitor (Supplementary Figure 3). Furthermore, secondary plots of K_{Mapp}/V_{maxapp} and $1/V_{maxapp}$ vs. [SH-11037] and [**7**] fit the curves expected for mixed-type inhibition (Supplementary Figure 4). The catalytic mechanism of sEH proceeds as a nucleophilic attack onto the epoxide substrate by an Asp residue, which results in a tetrahedral intermediate, requiring activated water to release the diol and regenerate free enzyme.[9] Given that sEH has two substrates (in our assay, the fluorogenic substrate 3-phenyl-cyano(6-methoxy-2-naphthalenyl)methyl ester-2-oxiraneacetic acid [PHOME] and water), and involves a covalent intermediate, it is possible that SH-11037 may bind and stabilize an enzyme species late in the catalytic cycle that is still

in conformational equilibrium with the free enzyme. SH-11037 binding in the active site of such an enzyme species may not compete with the substrates. Taken together, these findings indicate that SH-11037 represents a novel, distinct chemotype from known sEH inhibitors,[18] although interestingly, some other flavonoid natural products have previously been identified as mixed-type sEH inhibitors.[19]

After establishing SH-11037's *in vitro* inhibition of sEH activity, it was crucial to assess whether the previously documented antiangiogenic effects of SH-11037[6] were mediated through the inhibition of sEH in the L-CNV model. Therefore, we analyzed the lipid profiles of the retina/choroid layers from mice, at an acute timepoint three days after CNV induction and intravitreal injections of 10 μM SH-11037 or *t*-AUCB. Since DHA is the most abundant bioactive lipid in the eye,[15] DHA epoxy and dihydroxy metabolite levels were evaluated to investigate sEH activity *in vivo*. Interestingly, 19,20-epoxydocosapentaenoic acid (EDP) and its dihydroxy metabolite, 19,20-dihydroxydocosapentaenoic acid (DHDP) were the DHA metabolites most affected by sEH inhibition (Figure 2e). The ratio of 19,20-EDP to 19,20-DHDP decreased after induction of neovascularization, indicative of enhanced sEH activity under these conditions. However, this ratio was partially normalized after SH-11037 or *t*-AUCB treatment compared to the vehicle treated controls, indicating sEH inhibition *in vivo* (Figure 2f). Despite being less potent than *t*-AUCB *in vitro* (Figure 2a), SH-11037 performed comparably *in vivo* (Figure 2f), perhaps indicative of better ocular bioavailability than the existing inhibitor. To our knowledge, this is the first evidence that local sEH chemical inhibition can alter the lipid balance in the eye.

Given the significantly suppressed ratio of 19,20 EDP/DHDP after induction of CNV compared to the untreated control, suggestive of increased sEH activity, we investigated whether there are differences in sEH expression during neovascularization. Intriguingly, L-CNV treated mice demonstrated substantial upregulation of sEH in photoreceptor layers, both within and surrounding the neovascular lesion, compared to untreated eyes (Figure 3a). This upregulation of sEH in L-CNV was further confirmed in immunoblots of retina and choroid layers of laser-treated mouse eyes relative to untreated controls (Figure 3b). Co-immunostaining revealed co-localization of upregulated sEH levels with rod photoreceptors in the eyes of L-CNV mice compared to controls (Figure 3c, Supplementary Figure 5), but no overlap with markers of other retinal cell types, including retinal ganglion cells, horizontal cells, Müller glia, and cone photoreceptors (Supplementary Figures 5, 6, 7, 8). This increase in immunostaining corresponded to an increase in sEH activity in L-CNV eye lysates, which could be normalized by SH-11037 or compound **7** treatment (Figure 3d). Surprisingly, postmortem human wet AMD patients' eyes also revealed changed sEH expression in the central retina compared to age-matched controls: an increase in the staining pattern of sEH in the inner retina seen in age-matched control retina, and aberrant expression in some photoreceptors (Figure 3e; Supplementary Figure 9). Together, these data strongly suggest a role for retinal sEH in the CNV process both in mice and humans.

sEH is widely expressed in various tissues, with the highest levels of expression seen in liver, kidney, and brain in neuronal cell bodies and astrocytes.[20, 21] In mouse eye development it is expressed in Müller glial cells,[22] and in oxygen-induced retinopathy in neonatal mice, expression is seen in retinal ganglion cells, neovessels, and inner nuclear layer neurons.[23] Our data suggest a differential expression pattern in the adult mouse eye, especially under CNV

stress. Aged human eyes, in turn, have another pattern of expression, but this could also be a species difference: the rod-specific sEH expression seen in response to CNV in the rod-dominant, nocturnal murine eye might be expected to be shared by other cell types, as we observed, in the cone-dominant human macula.

Several studies have demonstrated potent antiangiogenic effects of DHA and its epoxides in the eye after genetic manipulation and/or dietary or *i.p.* administration,[22, 24–28] although a few studies showed proangiogenic effects.[23, 29, 30] To date however, inhibition of sEH using small molecules has only been tested in L-CNV using systemic administration through *i.p.* injections[28, 29], and showed antiangiogenic effects only when diet was supplemented with ω-3 fatty acids or their epoxides.[28] Given that the arachidonic acid pathway leading to EET formation is dominant systemically,[31] unlike in the eye, the effects of EDP buildup after systemic sEH inhibition might be partially offset by the concomitant proangiogenic EET buildup. Thus, local sEH inhibition is appealing.

To address this, we sought to test sEH inhibitors locally, using intravitreal injections, to minimize any systemic side effects and focus on understanding the effects of sEH in the eye specifically. We previously showed that SH-11037 was effective at doses ≥ 1 μM in this context.[6] Here, to validate sEH as a key target, we assessed the antiangiogenic effect of two chemically distinct small molecule inhibitors of sEH, *t*-AUCB (**5**) and compound **7**, in L-CNV (Figure 4). A single injection of either *t*-AUCB or compound **7** dose-dependently suppressed CNV lesion vascular volume compared to vehicle (Figure 4a-c), and comparable to the standard of care-equivalent anti-$VEGF_{164}$ antibody, suggesting indeed that sEH inhibition directly in the eye does not require ω-3 supplementation for antiangiogenic efficacy.

Additionally, in order to confirm our observations in a different model system, we tested *t*-AUCB and compound **7** in the choroidal sprouting assay, as an *ex vivo* model of CNV.[6] Interestingly, both *t*-AUCB and compound **7** suppressed the ability of choroidal tissues to form sprouts (Figure 4d-e).

The effect of ω-3 polyunsaturated fatty acids (PUFA) levels on choroidal neovascularization has been previously reported *in vivo* in the L-CNV model[24, 25] and in wet AMD patients.[32] Interestingly, in the retina of sEH knockout mice, pronounced changes in the levels of 19,20-DHDP, but not the epoxy metabolites of DHA, compared to wild-type control mice were observed.[22] Moreover, 19,20-DHDP could rescue the suppressed developmental retinal angiogenesis phenotype observed with these mice,[22] and as noted *i.p.* injections of 19,20-EDP suppressed CNV lesion volume in the L-CNV mouse model.[25, 28] While the explanation for the absence of changes in other EDPs after sEH inhibition or knockout is not clear, it is possible that the DHA epoxy (19,20-EDP) and diol (19,20-DHDP) metabolites and the activity of sEH are the major factors underlying the observed changes in retinal and choroidal angiogenesis rather than DHA levels themselves. Despite the role of DHA in the eye, the variability in the circulating levels of DHA among individuals suggests that dietary intake of ω-3 PUFA would not be sufficient alone for the prevention or treatment of wet AMD.[32] Therefore, local small molecule inhibition of sEH is an appealing therapeutic approach of significant interest for wet AMD patients to augment DHA epoxy metabolite levels with or without dietary supplementation of ω-3 PUFA (Figure 4f).

In conclusion, our findings reveal not only the target of an antiangiogenic molecule and a novel chemotype for sEH inhibition, but also a central role for local sEH in ocular

neovascularization. Developing novel, ocular specific sEH-targeted therapies is a possible approach to complement or combine with the existing anti-VEGF medications to overcome their limitations and tackle multiple angiogenesis signaling pathways for improved treatment of wet AMD; we already showed that SH-11037 can synergize with an anti-VEGF antibody in L-CNV.[6] Additionally, sEH and its inhibition using small molecules such as SH-11037 could be further investigated in other ocular neovascular diseases including PDR and ROP.

ACKNOWLEDGEMENTS

We thank M. Sturek for the porcine brain, and K. Maddipati at the Wayne State University Lipidomics Core, supported in part by NIH/NCRR S10RR027926. T.W.C. acknowledges support from the International Retinal Research Foundation, the Retina Research Foundation, the BrightFocus Foundation, NIH/NEI R01EY025641, and an unrestricted grant from Research to Prevent Blindness, Inc. S.-Y.S. was supported by the Pioneer Research Center Program through the National Research Foundation of Korea (NRF-2014M3C1A3054139) and the Korea Health Technology R&D Project through the Korea Health Industry Development Institute (KHIDI-HI14C1135). This publication was also made possible in part by R01EY018358 (M.E.B.), NIH/NCATS UL1TR001108 and KL2TR001106.

METHODS

Details of experimental procedures are provided in the Supporting Information.

ASSOCIATED CONTENT

Supporting Information Available: This material is available free of charge *via* the Internet. Experimental procedures, Supplementary Figures 1−9, and Supplementary Movie.

AUTHOR INFORMATION

R.S.S., B.L., S.Y.S., X.F., and T.W.C. are named inventors on patent applications related to the current work. No other authors declare competing financial interests.

REFERENCES

1. Das, A., and McGuire, P. G. (2003) Retinal and choroidal angiogenesis: pathophysiology and strategies for inhibition, *Prog. Retin. Eye Res. 22*, 721–748.

2. Prasad, P. S., Schwartz, S. D., and Hubschman, J. P. (2010) Age-related macular degeneration: current and novel therapies, *Maturitas 66*, 46–50.

3. Falavarjani, K. G., and Nguyen, Q. D. (2013) Adverse events and complications associated with intravitreal injection of anti-VEGF agents: a review of literature, *Eye 27*, 787–794.

4. Lux, A., Llacer, H., Heussen, F. M., and Joussen, A. M. (2007) Non-responders to bevacizumab (Avastin) therapy of choroidal neovascular lesions, *Br. J. Ophthalmol. 91*, 1318–1322.

5. Basavarajappa, H. D., Lee, B., Lee, H., Sulaiman, R. S., An, H., Magana, C., Shadmand, M., Vayl, A., Rajashekhar, G., Kim, E. Y., Suh, Y. G., Lee, K., Seo, S. Y., and Corson, T. W. (2015) Synthesis and biological evaluation of novel homoisoflavonoids for retinal neovascularization, *J. Med. Chem. 58*, 5015–5027.

6. Sulaiman, R. S., Merrigan, S., Quigley, J., Qi, X., Lee, B., Boulton, M. E., Kennedy, B., Seo, S. Y., and Corson, T. W. (2016) A novel small molecule ameliorates ocular neovascularisation and synergises with anti-VEGF therapy, *Sci. Rep. 6*, 25509.

7. Grossniklaus, H. E., Kang, S. J., and Berglin, L. (2010) Animal models of choroidal and retinal neovascularization, *Prog Retinal Eye Res 29*, 500–519.

8. Lee, B., Sun, W., Lee, H., Basavarajappa, H., Sulaiman, R. S., Sishtla, K., Fei, X., Corson, T. W., and Seo, S. Y. (2016) Design, synthesis and biological evaluation of photoaffinity probes of antiangiogenic homoisoflavonoids, *Bioorg. Med. Chem. Lett. 26*, 4277–4281.

9. Borhan, B., Jones, A. D., Pinot, F., Grant, D. F., Kurth, M. J., and Hammock, B. D. (1995) Mechanism of soluble epoxide hydrolase. Formation of an alpha-hydroxy ester-enzyme intermediate through Asp-333, *J. Biol. Chem. 270*, 26923–26930.

10. Harris, T. R., and Hammock, B. D. (2013) Soluble epoxide hydrolase: gene structure, expression and deletion, *Gene 526*, 61–74.

11. Zhang, G., Kodani, S., and Hammock, B. D. (2014) Stabilized epoxygenated fatty acids regulate inflammation, pain, angiogenesis and cancer, *Prog. Lipid Res. 53*, 108–123.

12. Panigrahy, D., Edin, M. L., Lee, C. R., Huang, S., Bielenberg, D. R., Butterfield, C. E., Barnes, C. M., Mammoto, A., Mammoto, T., Luria, A., Benny, O., Chaponis, D. M., Dudley, A. C., Greene, E. R., Vergilio, J. A., Pietramaggiori, G., Scherer-Pietramaggiori, S. S., Short, S. M., Seth, M., Lih, F. B., Tomer, K. B., Yang, J., Schwendener, R. A., Hammock, B. D., Falck, J. R., Manthati, V. L., Ingber, D. E., Kaipainen, A., D'Amore, P. A., Kieran, M. W., and Zeldin, D. C. (2012) Epoxyeicosanoids stimulate multiorgan metastasis and tumor dormancy escape in mice, *J. Clin. Invest. 122*, 178–191.

13. Morisseau, C., and Hammock, B. D. (2013) Impact of soluble epoxide hydrolase and epoxyeicosanoids on human health, *Annu. Rev. Pharmacol. Toxicol. 53*, 37–58.

14. Lazaar, A. L., Yang, L., Boardley, R. L., Goyal, N. S., Robertson, J., Baldwin, S. J., Newby, D. E., Wilkinson, I. B., Tal-Singer, R., Mayer, R. J., and Cheriyan, J. (2016) Pharmacokinetics, pharmacodynamics and adverse event profile of GSK2256294, a novel soluble epoxide hydrolase inhibitor, *Br. J. Clin. Pharmacol. 81*, 971–979.

15. Arterburn, L. M., Hall, E. B., and Oken, H. (2006) Distribution, interconversion, and dose response of n-3 fatty acids in humans, *Am. J. Clin. Nutr. 83*, 1467S–1476S.

16. Fromel, T., Jungblut, B., Hu, J., Trouvain, C., Barbosa-Sicard, E., Popp, R., Liebner, S., Dimmeler, S., Hammock, B. D., and Fleming, I. (2012) Soluble epoxide hydrolase regulates hematopoietic progenitor cell function via generation of fatty acid diols, *Proceedings of the National Academy of Sciences of the United States of America 109*, 9995–10000.

17. Shen, H. C., Ding, F. X., Deng, Q., Xu, S., Tong, X., Zhang, X., Chen, Y., Zhou, G., Pai, L. Y., Alonso-Galicia, M., Roy, S., Zhang, B., Tata, J. R., Berger, J. P., and Colletti, S. L. (2009) A strategy of employing aminoheterocycles as amide mimics to identify novel, potent and bioavailable soluble epoxide hydrolase inhibitors, *Bioorg. Med. Chem. Lett. 19*, 5716–5721.

18. Shen, H. C., and Hammock, B. D. (2012) Discovery of inhibitors of soluble epoxide hydrolase: a target with multiple potential therapeutic indications, *J. Med. Chem. 55*, 1789–1808.

19. Thao, N. P., Luyen, B. T., Kim, J. H., Jo, A. R., Dat, N. T., Kiem, P. V., Minh, C. V., and Kim, Y. H. (2016) Identification, characterization, kinetics, and molecular docking of flavonoid constituents from *Archidendron clypearia* (Jack.) Nielsen leaves and twigs, *Bioorg. Med. Chem. 24*, 3125–3132.

20. Norwood, S., Liao, J., Hammock, B. D., and Yang, G. Y. (2010) Epoxyeicosatrienoic acids and soluble epoxide hydrolase: potential therapeutic targets for inflammation and its induced carcinogenesis, *Am J Transl Res 2*, 447–457.

21. Sura, P., Sura, R., Enayetallah, A. E., and Grant, D. F. (2008) Distribution and expression of soluble epoxide hydrolase in human brain, *J. Histochem. Cytochem. 56*, 551–559.

22. Hu, J., Popp, R., Fromel, T., Ehling, M., Awwad, K., Adams, R. H., Hammes, H. P., and Fleming, I. (2014) Müller glia cells regulate Notch signaling and retinal angiogenesis via the generation of 19,20-dihydroxydocosapentaenoic acid, *J. Exp. Med. 211*, 281–295.

23. Shao, Z., Fu, Z., Stahl, A., Joyal, J. S., Hatton, C., Juan, A., Hurst, C., Evans, L., Cui, Z., Pei, D., Gong, Y., Xu, D., Tian, K., Bogardus, H., Edin, M. L., Lih, F., Sapieha, P., Chen, J., Panigrahy, D., Hellstrom, A., Zeldin, D. C., and Smith, L. E. (2014) Cytochrome P450 2C8 ω3-long-chain polyunsaturated fatty acid metabolites increase mouse retinal pathologic neovascularization--brief report, *Arterioscler. Thromb. Vasc. Biol. 34*, 581–586.

24. Moghaddam-Taaheri, S., Agarwal, M., Amaral, J., Fedorova, I., Agron, E., Salem, N., Jr., Chew, E., and Becerra, S. P. (2011) Effects of docosahexaenoic acid in preventing experimental choroidal neovascularization in rodents, *J. Clin. Exp. Ophthalmol. 2*, 187.

25. Yanai, R., Mulki, L., Hasegawa, E., Takeuchi, K., Sweigard, H., Suzuki, J., Gaissert, P., Vavvas, D. G., Sonoda, K. H., Rothe, M., Schunck, W. H., Miller, J. W., and Connor, K. M. (2014) Cytochrome P450-generated metabolites derived from omega-3 fatty acids attenuate neovascularization, *Proc. Natl. Acad. Sci. U. S. A. 111*, 9603–9608.

26. Stahl, A., Sapieha, P., Connor, K. M., Sangiovanni, J. P., Chen, J., Aderman, C. M., Willett, K. L., Krah, N. M., Dennison, R. J., Seaward, M. R., Guerin, K. I., Hua, J., and Smith, L. E. (2010) Short communication: PPAR gamma mediates a direct antiangiogenic effect of omega 3-PUFAs in proliferative retinopathy, *Circ. Res. 107*, 495–500.

27. Connor, K. M., SanGiovanni, J. P., Lofqvist, C., Aderman, C. M., Chen, J., Higuchi, A., Hong, S., Pravda, E. A., Majchrzak, S., Carper, D., Hellstrom, A., Kang, J. X., Chew, E. Y., Salem, N., Jr., Serhan, C. N., and Smith, L. E. (2007) Increased dietary intake of omega-3-polyunsaturated fatty acids reduces pathological retinal angiogenesis, *Nat. Med. 13*, 868–873.

28. Hasegawa, E., Inafuku, S., Mulki, L., Okunuki, Y., Yanai, R., Smith, K. E., Kim, C. B., Klokman, G., Bielenberg, D. R., Puli, N., Falck, J. R., Husain, D., Miller, J. W., Edin, M. L., Zeldin, D. C., Lee, K. S. S., Hammock, B. D., Schunck, W. H., and Connor, K. M. (2017) Cytochrome P450 monooxygenase lipid metabolites are significant second messengers in the resolution of choroidal neovascularization, *Proc. Natl. Acad. Sci. U. S. A.*

29. Gong, Y., Fu, Z., Edin, M. L., Liu, C. H., Wang, Z., Shao, Z., Fredrick, T. W., Saba, N. J., Morss, P. C., Burnim, S. B., Meng, S. S., Lih, F. B., Lee, K. S., Moran, E. P., SanGiovanni, J. P., Hellstrom, A., Hammock, B. D., Zeldin, D. C., and Smith, L. E. (2016) Cytochrome P450 oxidase 2C inhibition adds to omega-3 long-chain polyunsaturated fatty acids protection against retinal and choroidal neovascularization, *Arterioscler. Thromb. Vasc. Biol. 36*, 1919–1927.

30. Gong, Y., Shao, Z., Fu, Z., Edin, M. L., Sun, Y., Liegl, R. G., Wang, Z., Liu, C. H., Burnim, S. B., Meng, S. S., Lih, F. B., SanGiovanni, J. P., Zeldin, D. C., Hellstrom, A., and

Smith, L. E. (2016) Fenofibrate inhibits cytochrome P450 epoxygenase 2c activity to suppress pathological ocular angiogenesis, *EBioMedicine 13*, 201–211.

31. Wang, W., Zhu, J., Lyu, F., Panigrahy, D., Ferrara, K. W., Hammock, B., and Zhang, G. (2014) omega-3 polyunsaturated fatty acids-derived lipid metabolites on angiogenesis, inflammation and cancer, *Prostaglandins Other Lipid Mediat. 113–115*, 13–20.

32. Merle, B. M., Benlian, P., Puche, N., Bassols, A., Delcourt, C., Souied, E. H., and Nutritional A. M. D. Treatment Study Group. (2014) Circulating omega-3 fatty acids and neovascular age-related macular degeneration, *Invest. Ophthalmol. Vis. Sci. 55*, 2010–2019.

32. Souied, E. H., Delcourt, C., Querques, G., Bassols, A., Merle, B., Zourdani, A., Smith, T., Benlian, P., and Nutritional A. M. D. Treatment Study Group. (2013) Oral docosahexaenoic acid in the prevention of exudative age-related macular degeneration: the Nutritional AMD Treatment 2 study, *Ophthalmology 120*, 1619–1631.

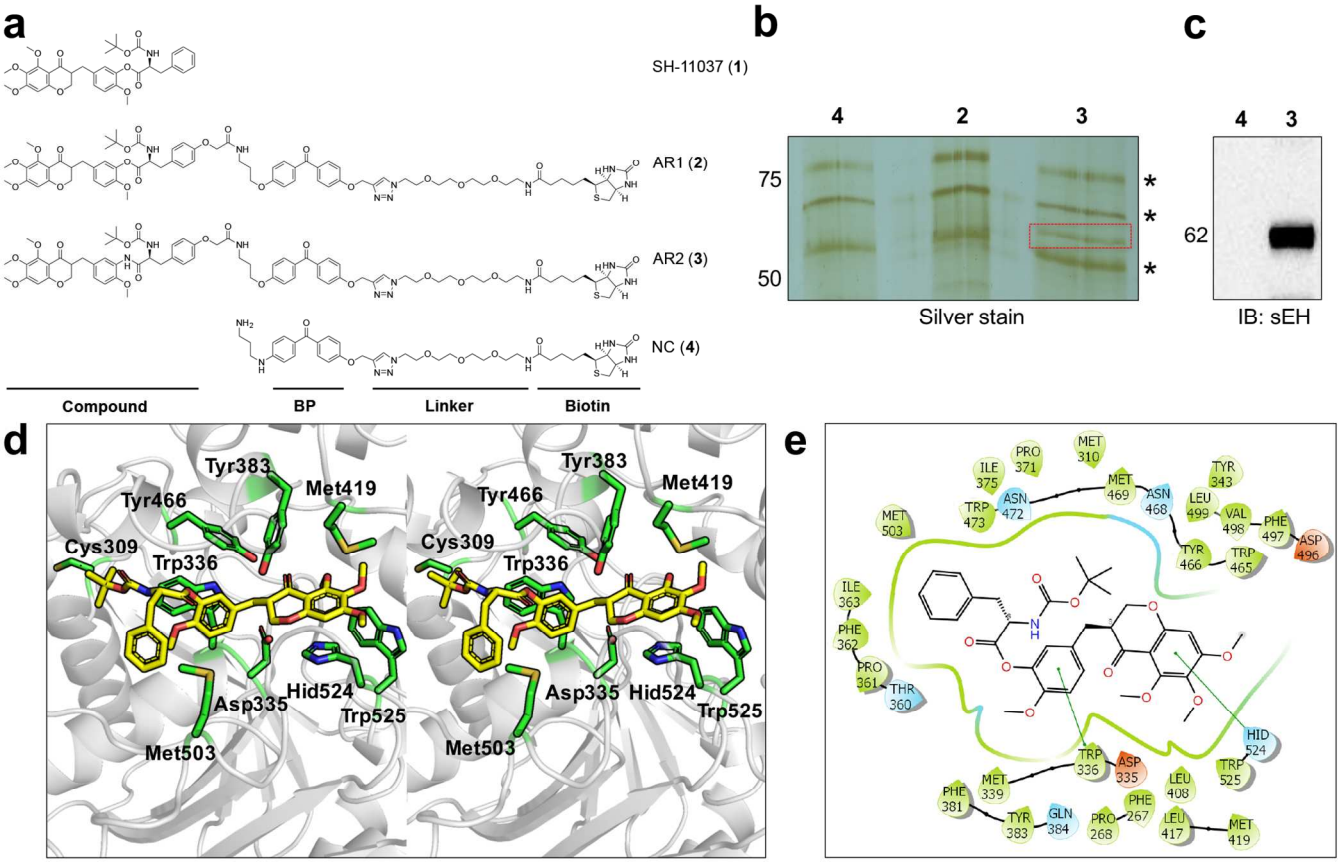

FIGURES

Figure 1. Soluble epoxide hydrolase (sEH) is a target of antiangiogenic homoisoflavonoid SH-11037. a) Structures of SH-11037 (**1**), ester affinity reagent (**2**), amide affinity reagent (**3**), and negative control reagent (**4**). BP, benzophenone moiety. b) Proteins pulled down with indicated reagents were separated by SDS-PAGE and silver stained, then identified by mass spectrometry. A unique band was present in pulldown with **3** but not **4**, *red box*; *asterisks* represent non-specific bands. c) Immunoblot of pulled down protein using antibody against sEH. Silver-stained gel and immunoblot are representatives from at least two independent experiments. d) SH-11037 (*yellow*) docks in the substrate-binding cleft of sEH, as shown in this stereo view. Key residues are shown in *green*. e) 2D interaction diagram for docked SH-11037. The protein "pocket" is displayed with a line around the ligand, colored with the color of the nearest protein residue. The π-π stacking interactions are shown as *green* lines.

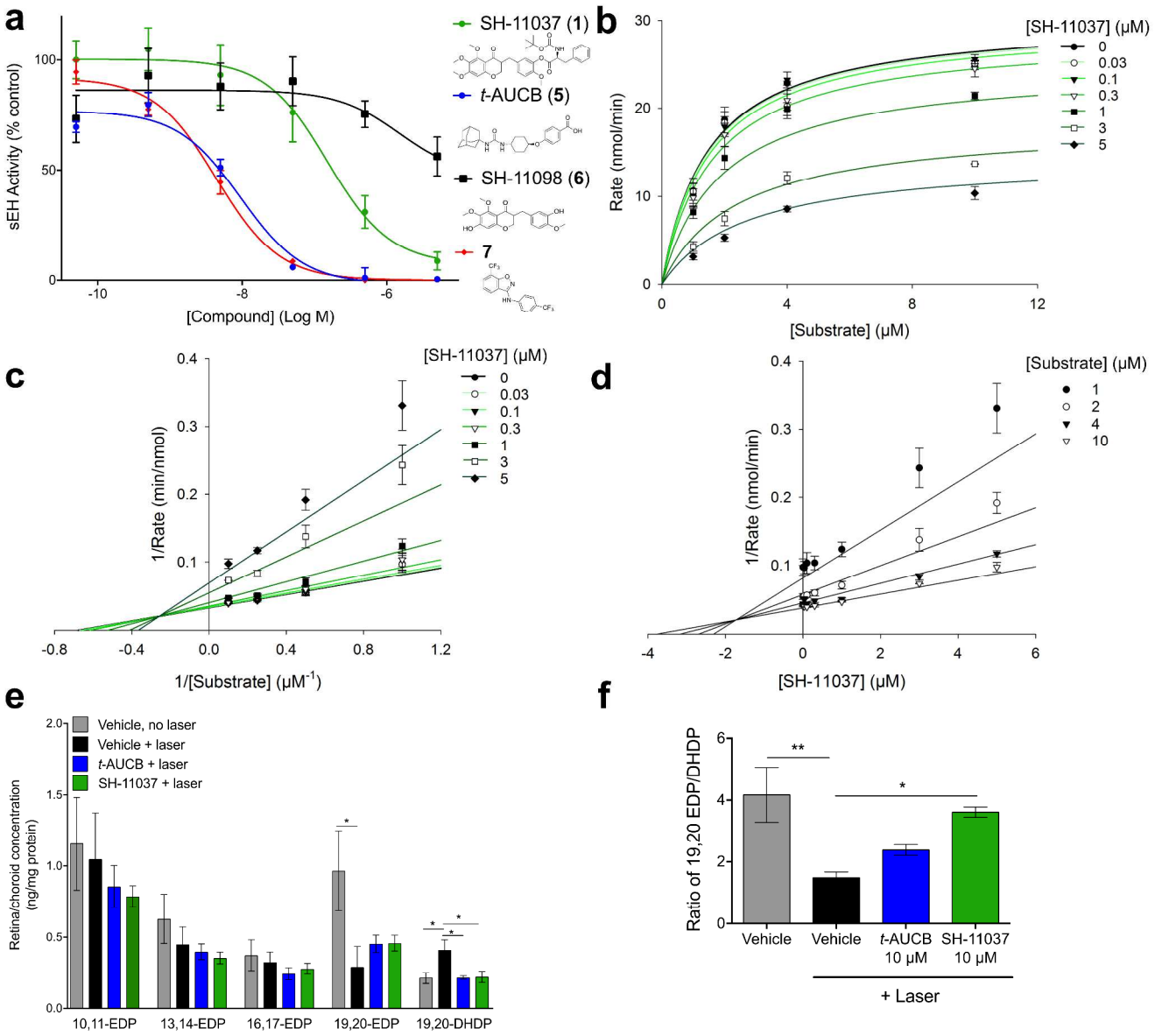

Figure 2. SH-11037 is an sEH inhibitor. a) SH-11037 (**1**) but not its inactive analog SH-11098 (**6**) significantly suppressed sEH enzymatic activity *in vitro*, IC_{50} = 0.15 μM (SH-11098 IC_{50} > 10 μM). The specific sEH inhibitors *t*-AUCB (**5**) and compound **7** were used as positive controls, IC_{50} = 9.5 nM for each. Mean ± SEM from triplicate wells shown. b) Michaelis-Menten kinetic response plot for sEH-mediated hydrolysis of fluorescent substrate, PHOME, for varying SH-11037 concentrations. Mean ± SEM from triplicate wells shown. c) Lineweaver-Burk plot of these data suggests mixed-type inhibition. d) Dixon plot further supports mixed-type inhibition. e) Lipid profile of retina/choroid for DHA-related metabolites from L-CNV (three days post-laser) or control mice treated with vehicle, 10 μM *t*-AUCB, or 10 μM SH-11037. EDP, epoxydocosapentaenoic acids; DHDP, dihydroxydocosapentaenoic acids. f) The ratio of 19,20 EDP/DHDP between different treatment conditions and vehicle only (no laser) control mice indicates increased sEH levels/activity three days following laser induction compared to no laser control, ***P*<0.01, and a significant sEH inhibition by SH-11037, **P*<0.05 vs. vehicle.

One-way ANOVA, Dunnett's post hoc tests. Mean ± SEM, n = 5 mice/treatment. Activity assay and kinetic analyses are representatives from at least two independent experiments.

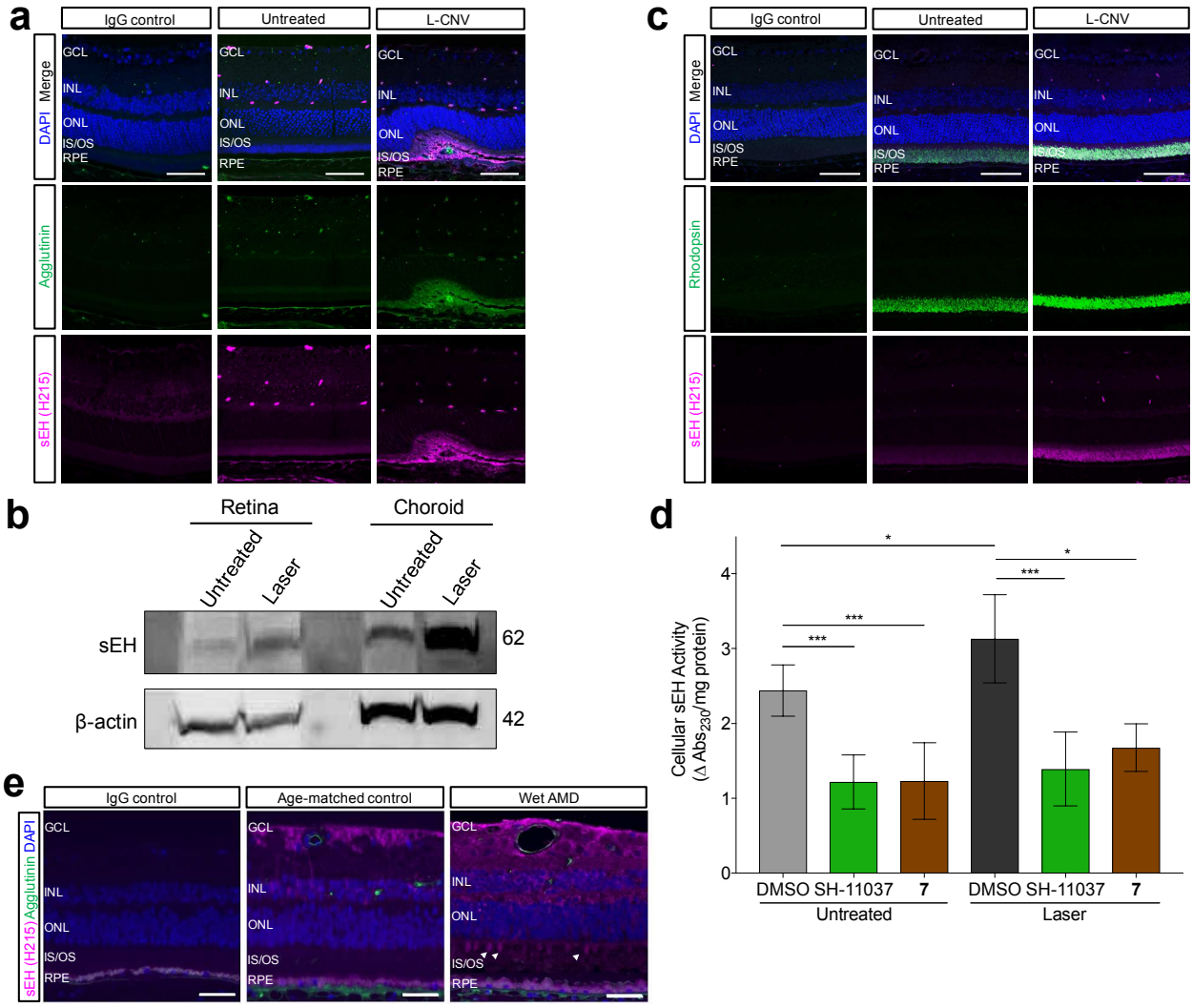

Figure 3. sEH is upregulated in the eyes of mice and humans undergoing neovascularization. a) Representative images of retinal sections from L-CNV and control eyes stained with DAPI (*blue*), agglutinin for vasculature (*green*), and sEH (*magenta*), showing upregulation of sEH in the outer retina in L-CNV sections three days post-laser. b) Immunoblot of sEH protein levels in mouse retina and choroid sections of laser treated mouse eyes three days post-laser compared to untreated controls; β-actin is a loading control. Pooled eyes from two independently-treated animals per condition. c) Representative images of retinal sections from L-CNV (three days post-laser) and control eyes stained with DAPI (*blue*), sEH (*magenta*), and rod marker rhodopsin (*green*), showing co-localization of upregulated sEH with rod photoreceptors. d) sEH activity is upregulated in L-CNV eye tissue (**P*<0.05) and normalized by 20 μM SH-11037 or **7** treatment (****P*<0.001), as indicated in a *trans*-stilbene oxide enzymatic activity assay performed three days post-laser. Mean ± SEM, ANOVA with Tukey's post hoc tests. Pooled data from three experiments, n = 2–3 animals per condition per experiment. e) Representative images of central retinal sections from eyes of human wet AMD patients (78 years old) and age-matched controls (68 years old). sEH is *magenta*, vasculature (FITC-agglutinin) is *green*, and nuclei (DAPI) are *blue*. In wet AMD, sEH is increased in the inner retina, and aberrantly expressed in some photoreceptors (*arrowheads*). Scale bars = 50

μm. IgG is a negative control with preimmune primary antibodies. GCL, ganglion cell layer; INL, inner nuclear layer; ONL, outer nuclear layer; IS/OS, photoreceptor inner segments/outer segments; RPE, retinal pigment epithelium.

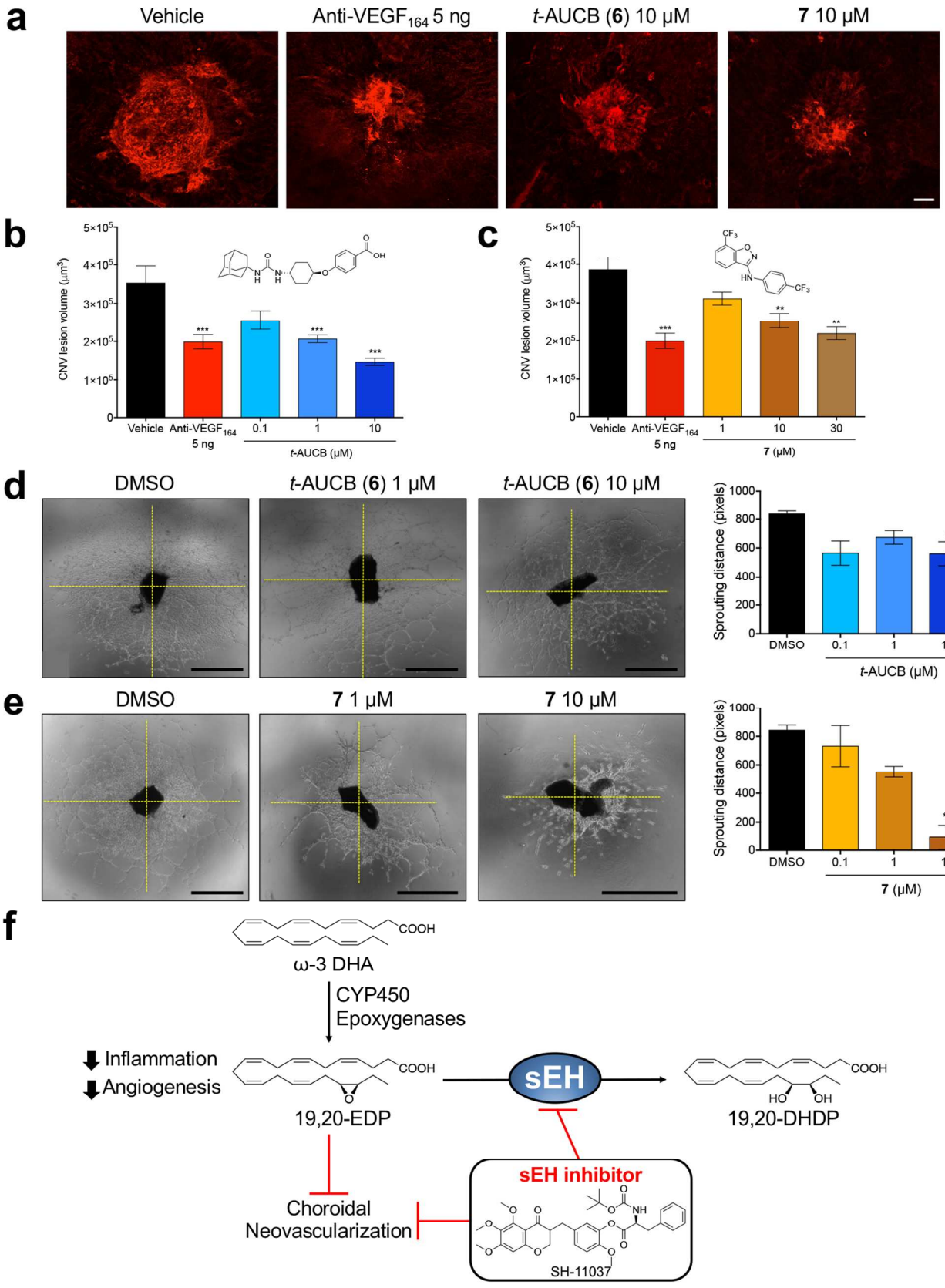

Figure 4. Local application of sEH inhibitors dose-dependently suppresses neovascularization.

a) Representative images from confocal microscopy of agglutinin stained CNV lesions 14 days post-laser, scale bar = 50 μm. b) & c) Dose-dependent inhibition of the volume of CNV lesions by b) *t*-AUCB (**6**) and c) sEH inhibitor **7** compared to vehicle control. Mean ± SEM, n = 6–15 animals/treatment (one eye per animal). **P*<0.05, ***P*<0.01, ****P*<0.001 compared to vehicle, one-way ANOVA, Dunnett's post hoc tests. d) & e) Inhibition of mouse choroidal sprouting *ex vivo* by d) *t*-AUCB (**6**) and e) sEH inhibitor **7** compared to vehicle control. Mean ± SEM, n = 4 eyes/treatment, representative data from at least two independent experiments. Axes for measurement of sprouting distance shown in *yellow*. Scale bars = 1 mm. **P*<0.05, ***P*<0.01 compared to vehicle, one-way ANOVA, Dunnett's post hoc tests. f) Summary of SH-11037's mechanism. By inhibiting sEH, SH-11037 decreases the formation of 19,20-DHDP (dihydroxydocosapentaenoic acid), and increases levels of docosahexaenoic acid (DHA)-derived 19,20-EDP (epoxydocosapentaenoic acid), with antiangiogenic effects.

TABLE OF CONTENTS GRAPHIC

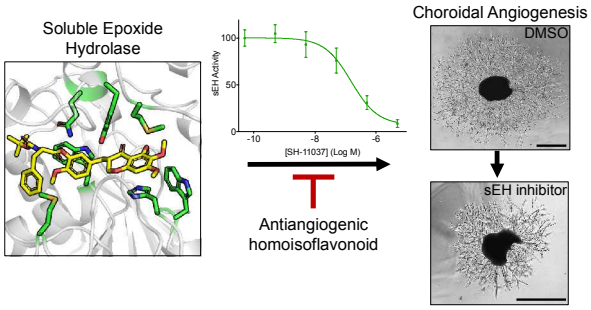

Supporting Information for:

Chemical proteomics reveals soluble epoxide hydrolase as a therapeutic target for ocular neovascularization

Rania S. Sulaiman,[†,‡,⊥] Bomina Park,[†,‡] Sardar Pasha Sheik Pran Babu,[†] Yubing Si,[§] Rakshin Kharwadkar,[§] Sayak K. Mitter,[†,▽] Bit Lee,[#] Wei Sun,[#] Xiaoping Qi, [†,▽] Michael E. Boulton,[†,▽] Samy O. Meroueh,[§,||] Xiang Fei,[#] Seung-Yong Seo,[*,#] Timothy W. Corson[*,†,‡,§,||]

[†]Eugene and Marilyn Glick Eye Institute, Department of Ophthalmology, [‡]Department of Pharmacology and Toxicology, [§]Department of Biochemistry and Molecular Biology, [||]Melvin and Bren Simon Cancer Center, Indiana University School of Medicine, Indianapolis, Indiana 46202, United States of America. [⊥]Department of Biochemistry, Faculty of Pharmacy, Cairo University, Cairo 12613, Egypt. [#]College of Pharmacy, Gachon University, Incheon 21936, South Korea. [▽]Department of Ophthalmology, University of Alabama Birmingham, Birmingham, Alabama 35294, United States of America

*Corresponding authors. E-mail: tcorson@iu.edu
Address: 1160 West Michigan Street, Indianapolis, IN 46202 USA
E-mail: syseo@gachon.ac.kr
Address: 191 Hambakoero, Yeonsu-gu, Incheon, Korea 21936

TABLE OF CONTENTS

Accession	Description	Score	Coverage	# Unique Peptides	# Peptides	# PSMs	MW [kDa]
P00761	Trypsin OS=Sus scrofa PE=1 SV=1 - [TRYP_PIG]	168.82	54.98	7	7	56	24.4
F1S0L1	Uncharacterized protein OS=Sus scrofa GN=LOC100737113 PE=3 SV=2 - [F1S0L1_PIG]	83.66	17.26	6	7	24	51.5
Q6Q2C2	Bifunctional epoxide hydrolase 2 OS=Sus scrofa GN=EPHX2 PE=2 SV=1 - [HYES_PIG]	73.43	29.91	12	12	18	62.7
F2Z571	Uncharacterized protein OS=Sus scrofa GN=LOC100516352 PE=2 SV=1 - [F2Z571_PIG]	53.69	17.98	2	6	15	49.8
P02554	Tubulin beta chain OS=Sus scrofa PE=1 SV=1 - [TBB_PIG]	52.07	17.98	2	6	14	49.8
I3LDS3	Uncharacterized protein OS=Sus scrofa GN=LOC100519971 PE=3 SV=1 - [I3LDS3_PIG]	43.13	9.60	5	6	14	58.0
F1SGG3	Uncharacterized protein OS=Sus scrofa GN=KRT1 PE=3 SV=1 - [F1SGG3_PIG]	40.91	7.31	2	5	19	65.2
F2Z5T5	Tubulin alpha-1B chain OS=Sus scrofa GN=TUBA1B PE=3 SV=1 - [F2Z5T5_PIG]	39.96	25.06	1	7	11	50.1
F1SHC1	Uncharacterized protein OS=Sus scrofa GN=LOC100127131 PE=3 SV=1 - [F1SHC1_PIG]	38.21	25.17	1	7	10	49.9
I3LNT6	Uncharacterized protein OS=Sus scrofa GN=KRT77 PE=3 SV=1 - [I3LNT6_PIG]	37.49	5.34	1	3	19	62.3
I3LDM6	Uncharacterized protein OS=Sus scrofa GN=LOC100157304 PE=3 SV=1 - [I3LDM6_PIG]	31.25	8.24	3	6	10	65.1
F1SGG6	Uncharacterized protein (Fragment) OS=Sus scrofa GN=KRT5 PE=3 SV=2 - [F1SGG6_PIG]	23.32	10.25	4	6	8	63.4
F1SGG4	Uncharacterized protein OS=Sus scrofa PE=3 SV=2 - [F1SGG4_PIG]	21.37	8.45	1	4	7	53.3
F1SGI7	Uncharacterized protein (Fragment) OS=Sus scrofa GN=LOC100525745 PE=3 SV=2 - [F1SGI7_PIG]	17.16	6.89	2	4	6	65.1
F1RUN2	Serum albumin OS=Sus scrofa GN=ALB PE=4 SV=1 - [F1RUN2_PIG]	11.08	2.14	1	1	3	69.6

Supplementary Figure 1. Peptide mass fingerprinting analysis of proteins pulled down with an SH-11037 affinity reagent from a porcine brain lysate. EPHX2 was the top-scoring protein hit not also seen in a size-matched control sample (shared hits are colored *blue*).

a

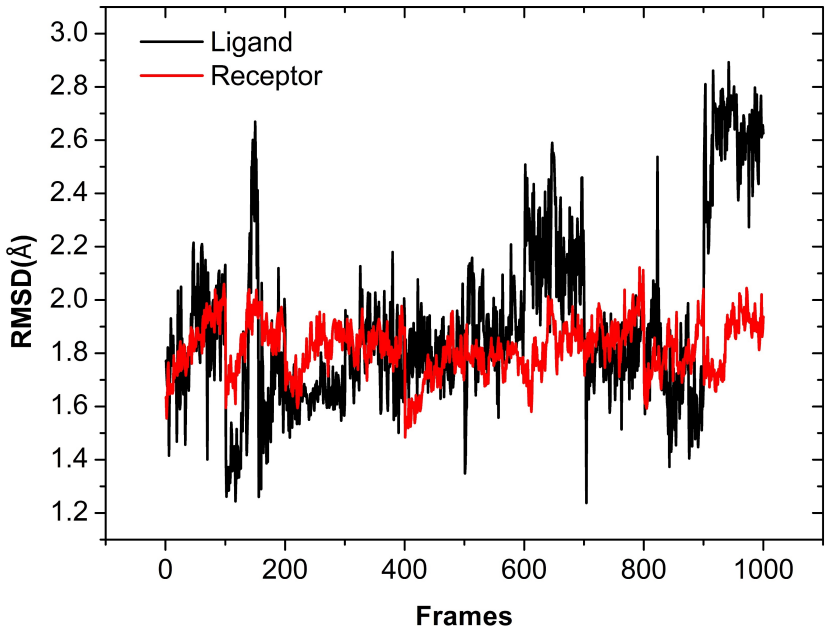

b

	ΔE_{VDW}	ΔE_{ELE}	ΔE_{GB}	ΔE_{SURF}	ΔE_{GBTOT}	$T\Delta S_{NMODE}$	ΔG_{MMGBSA}
Energy (kcal/mol)	-83.6±0.2	-30.5±0.2	57.9±1.1	-10.7±0.0	-66.9±0.2	-22.7±1.4	-44.1±0.2

Supplementary Figure 2. Molecular dynamics simulation results. (a) Root-mean-squared deviation (RMSD) of SH-11037 (ligand; black) and sEH (receptor; red) over the course of several nanoseconds of molecular dynamics simulations; see Supplementary Movie. (b) Free energy parameters calculated by MMPBSA, computed means ± SEM; see Experimental Procedures.

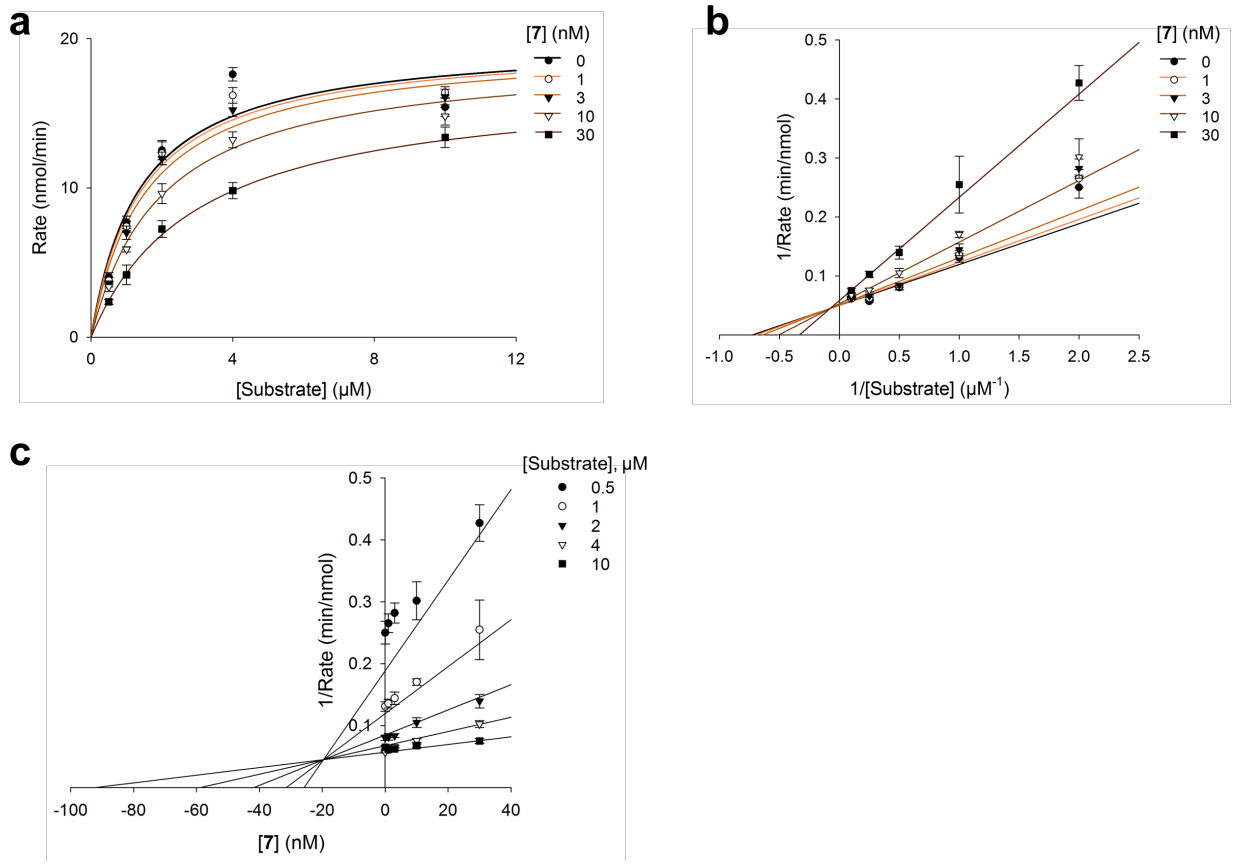

Supplementary Figure 3. Kinetic analysis for sEH inhibition by compound **7**. (a) Michaelis-Menten kinetic response plot for hydrolysis of fluorescent substrate, PHOME. (b) Lineweaver-Burk plot indicates mixed-type inhibition. (c) K_i = 19.6 ± 5.4 nM is illustrated on Dixon plot. Mean ± SEM, n = 3. Representative results from at least two independent experiments.

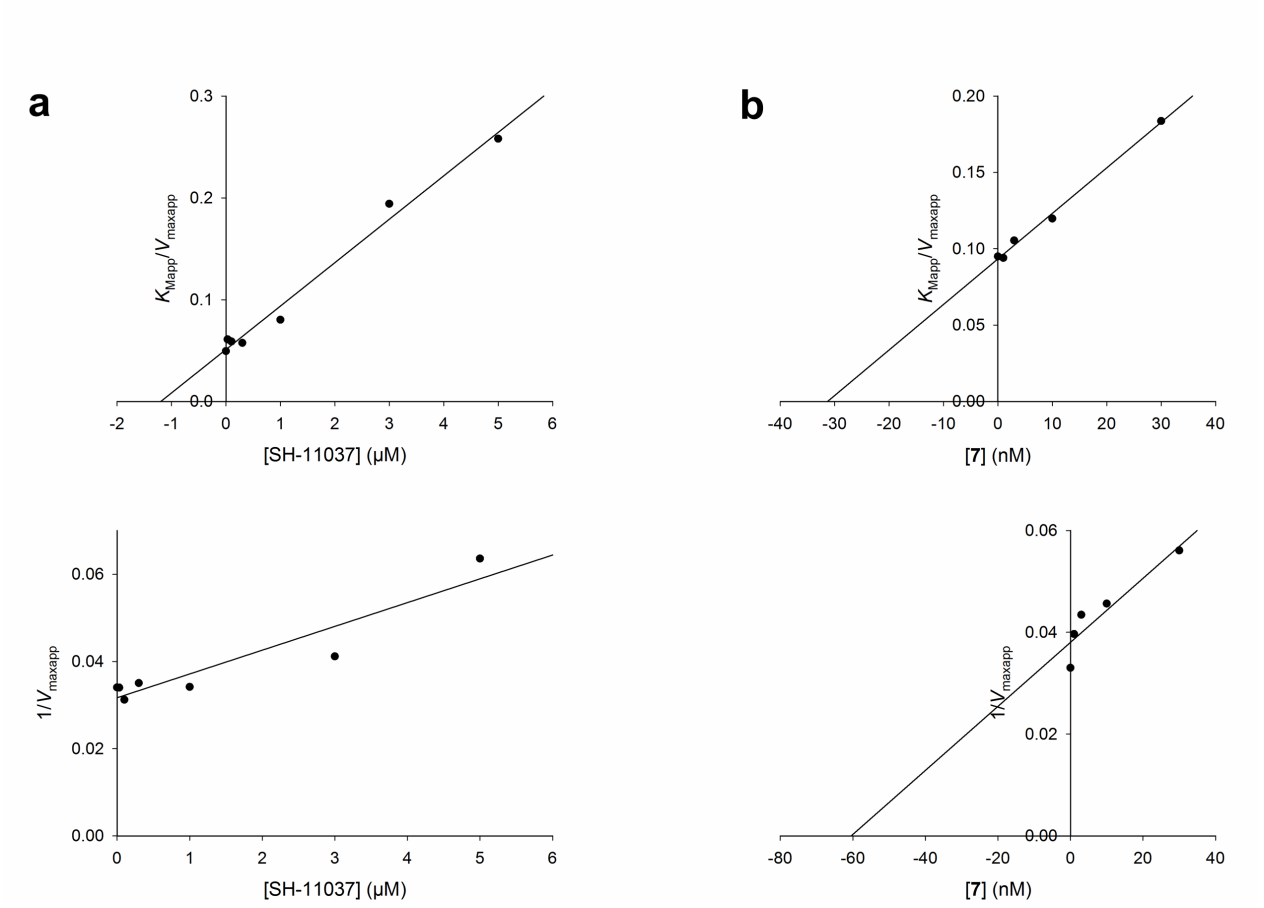

Supplementary Figure 4. Secondary plots for enzyme kinetic analyses. The apparent K_M/V_{max} data fit the expected profiles for mixed-type inhibition by SH-11037 and **7**. (a) K_{Mapp}/V_{maxapp} and $1/V_{maxapp}$ vs. [SH-11037]. (b) K_{Mapp}/V_{maxapp} and $1/V_{maxapp}$ vs. [**7**]. Representative results from at least two independent experiments.

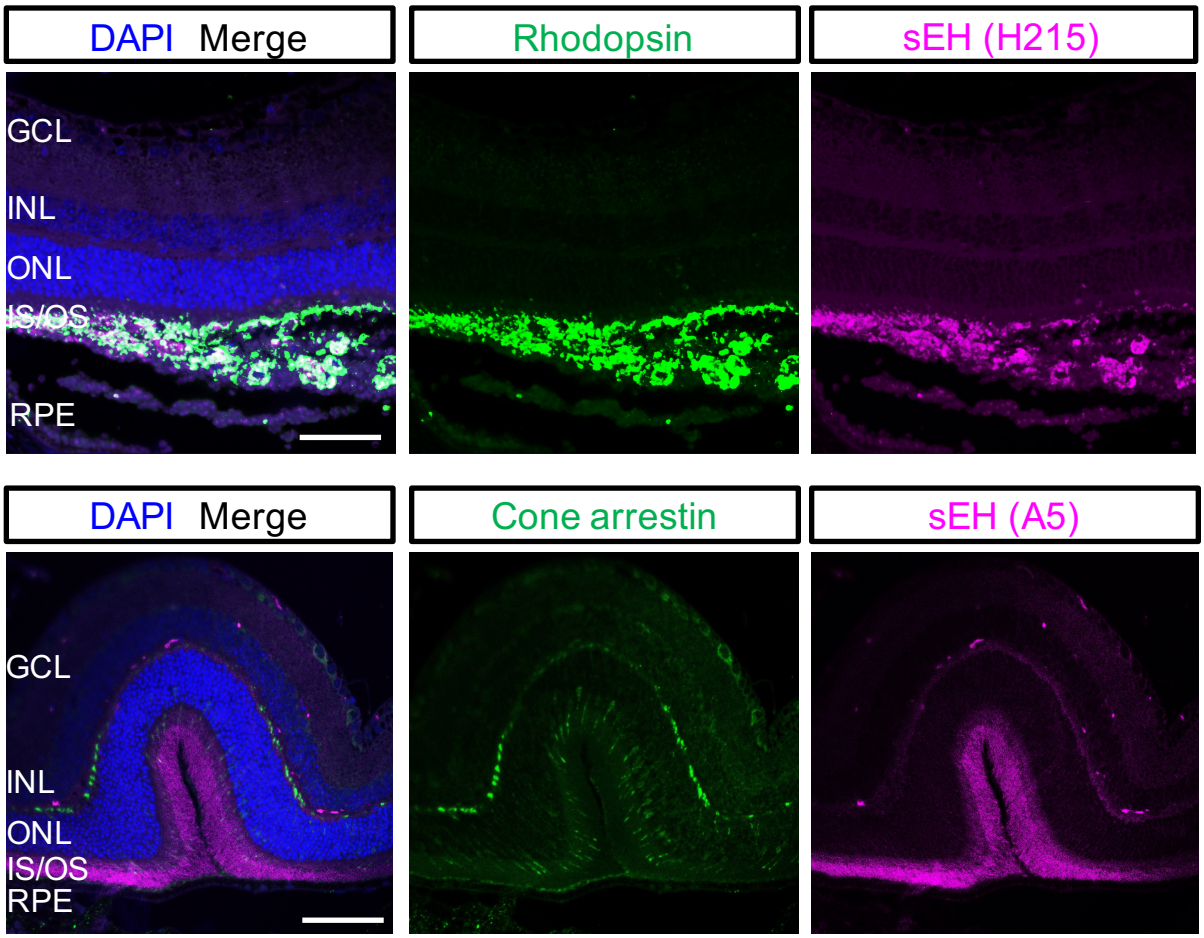

Supplementary Figure 5. Further evidence of sEH upregulation within L-CNV lesions 3 days post-laser-treatment, and co-staining with rod (rhodopsin) but not cone (arrestin) markers. sEH is magenta, cell type markers are green, and nuclei (DAPI) are blue. GCL, ganglion cell layer; INL, inner nuclear layer; ONL, outer nuclear layer; IS/OS, photoreceptor inner segments/outer segments; RPE, retinal pigment epithelium. Scale bars = 50 μm.

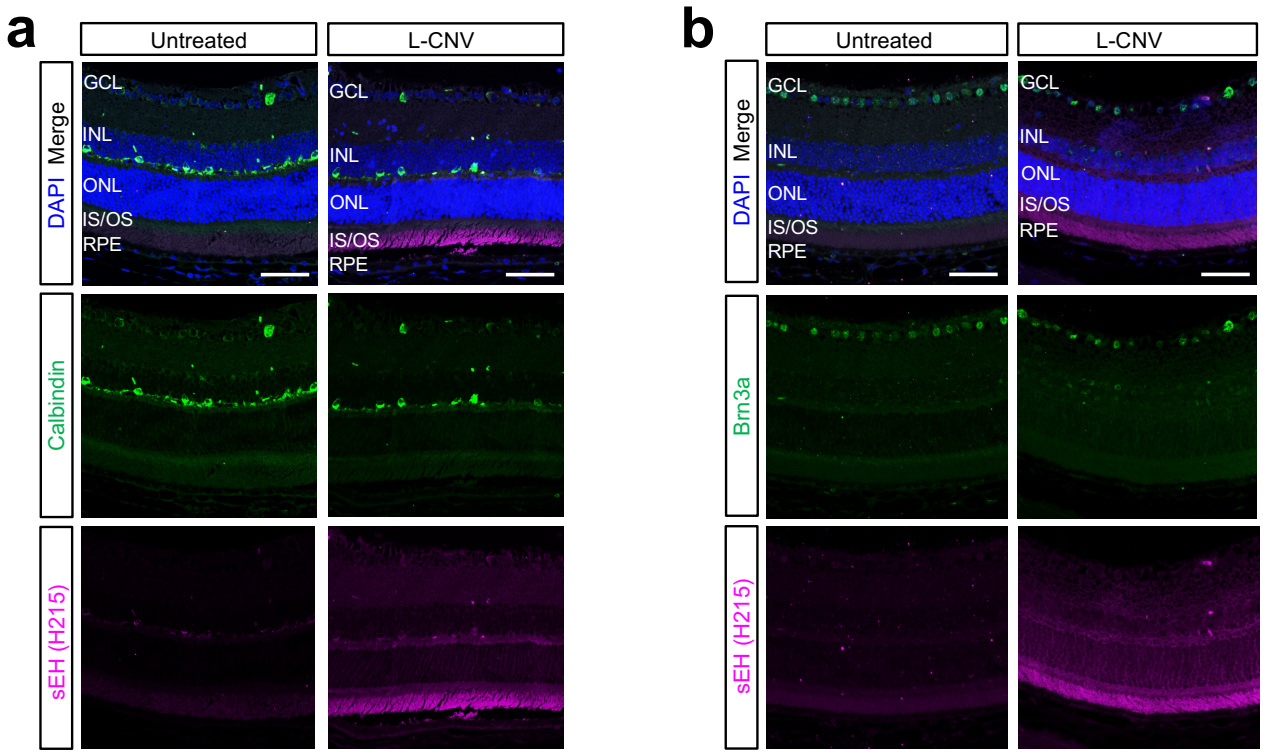

Supplementary Figure 6. sEH does not colocalize with markers of (a) horizontal cells (calbindin) or (b) retinal ganglion cells (Brn3a) in untreated C57BL/6 adult mouse eyes or in L-CNV eyes 3 days post-laser-treatment. sEH is magenta, cell type markers are green, and nuclei (DAPI) are blue. GCL, ganglion cell layer; INL, inner nuclear layer; ONL, outer nuclear layer; IS/OS, photoreceptor inner segments/outer segments; RPE, retinal pigment epithelium. Scale bars = 50 μm.

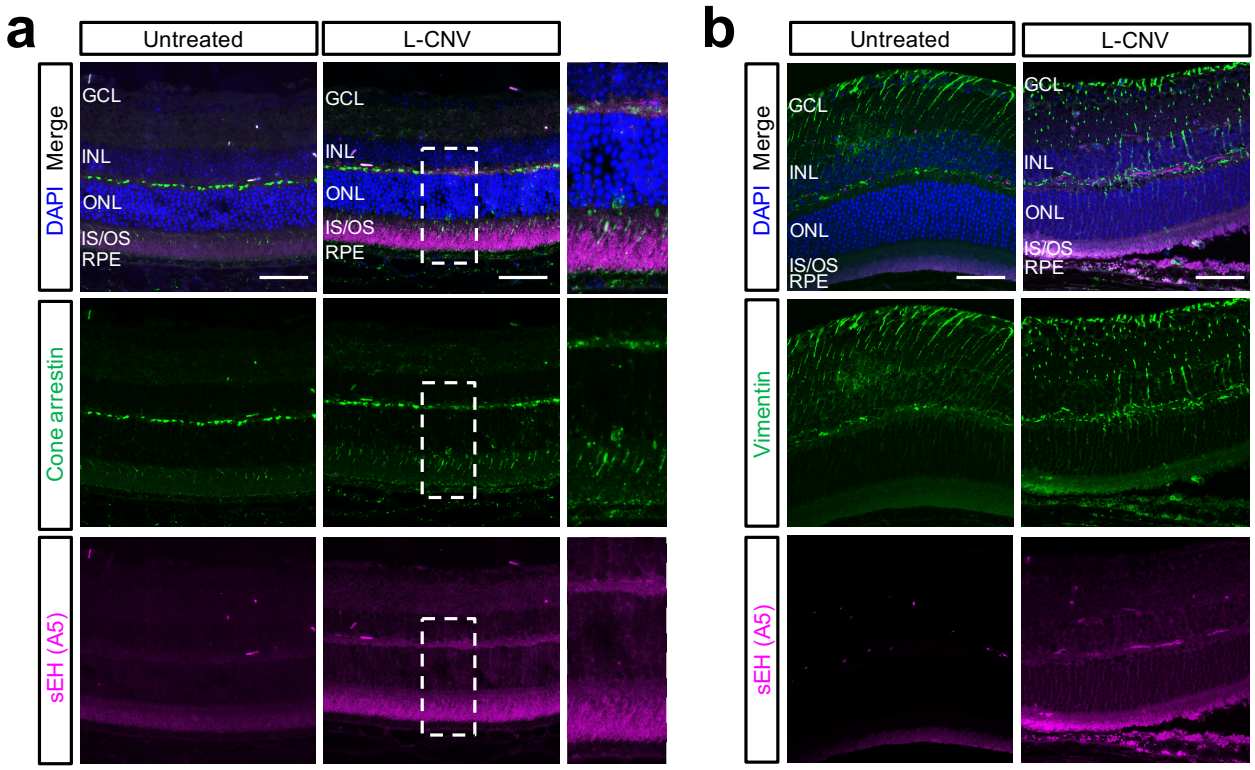

Supplementary Figure 7. sEH does not colocalize with markers of (a) cone photoreceptors (cone arrestin) or (b) Müller glia (vimentin) in untreated C57BL/6 adult mouse eyes or in L-CNV eyes, 3 days post-laser-treatment. Inset shows magnification of area marked by dotted lines. sEH is magenta, cell type markers are green, and nuclei (DAPI) are blue. GCL, ganglion cell layer; INL, inner nuclear layer; ONL, outer nuclear layer; IS/OS, photoreceptor inner segments/outer segments; RPE, retinal pigment epithelium. Scale bars = 50 μm.

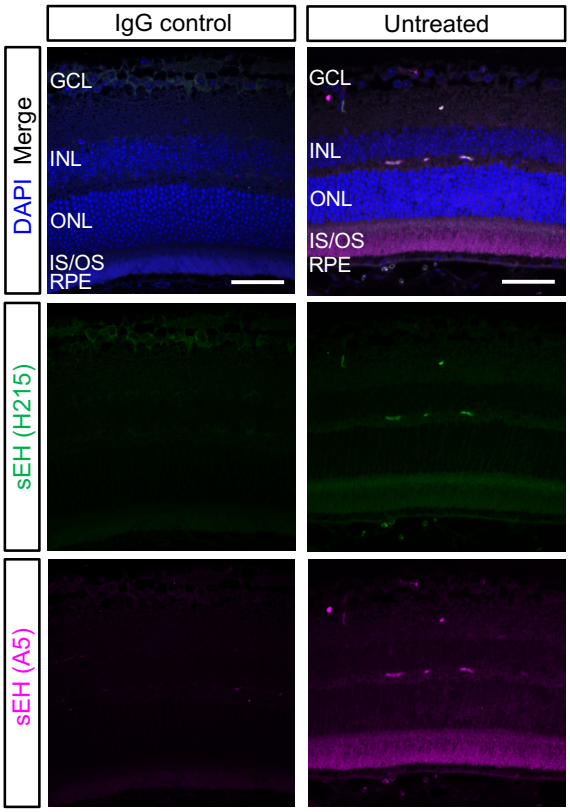

Supplementary Figure 8. Validation of sEH antibodies. A5 (magenta) is a mouse monoclonal antibody against sEH, while H215 (green) is a rabbit polyclonal antibody against sEH. Both antibodies show a similar staining pattern in murine retina, indicative of specificity for the target protein. GCL, ganglion cell layer; INL, inner nuclear layer; ONL, outer nuclear layer; IS/OS, photoreceptor inner segments/outer segments; RPE, retinal pigment epithelium. Scale bars = 50 μm.

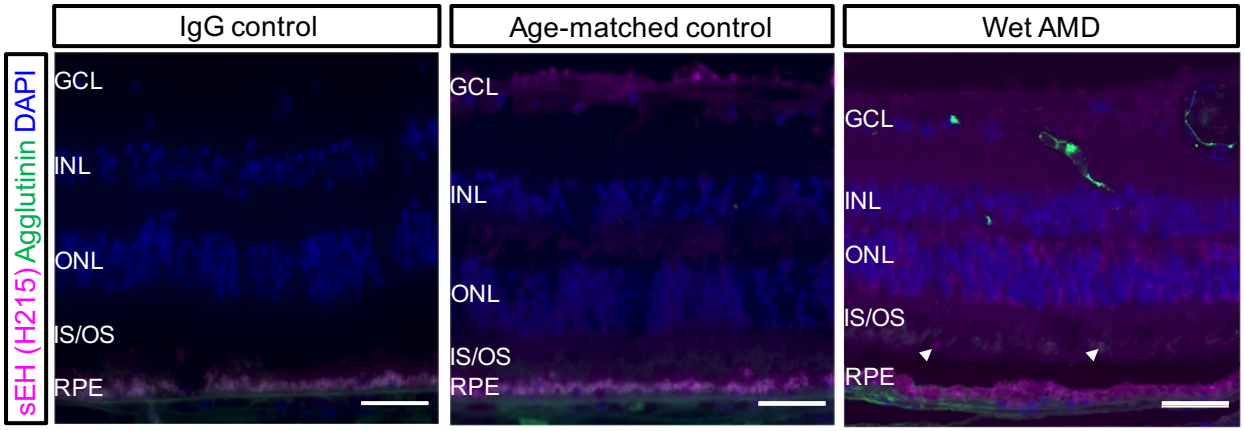

Supplementary Figure 9. Further example of differential sEH staining in the central retina of human wet AMD eyes (68 years old) versus age-matched controls (78 years old). sEH is magenta, vasculature (FITC-agglutinin) is green, and nuclei (DAPI) are blue. In wet AMD, sEH is increased in the inner retina, and aberrantly expressed in some photoreceptors (arrowheads). GCL, ganglion cell layer; INL, inner nuclear layer; ONL, outer nuclear layer; IS/OS, photoreceptor inner segments/outer segments; RPE, retinal pigment epithelium. Scale bars = 50 μm.

EXPERIMENTAL PROCEDURES

Preparation of Photoaffinity Reagents. Photoaffinity reagents were synthesized as described,[1] with purity confirmed as >95% by HPLC. For pulldowns, Neutravidin agarose beads (1 mL of 50% (v/v) slurry) were washed three times in buffer A (25 mM Tris-HCl pH 7.4, 150 mM NaCl, 2.5 mM sodium pyrophosphate, 1 mM phenylmethylsulfonyl fluoride (PMSF), 0.1 mM sodium orthovanadate, 10 μg/mL aprotinin and 10 μg/mL leupeptin). The beads were then incubated with 75 μM affinity reagents **2**, **3**, or **4** dissolved in DMSO (final DMSO concentration <0.1% (v/v)) and diluted in this buffer, overnight at 4°C with rotation. The beads were blocked using 1 mM biotin solution prepared in buffer A for 1 hour followed by incubation with 1 mg/mL cytochrome *c* solution for 1 hour at 4°C. The beads were then washed three times with buffer A and resuspended in 1 mL.

Photoaffinity Pulldown Experiments. Flash-frozen porcine brain (20 g) obtained from the Purdue-Indiana University School of Medicine Comparative Medicine Program was homogenized in 50 mL buffer A using a tissue homogenizer. The homogenate was centrifuged and sonicated. The lysate was then centrifuged at 11,000×*g* for 30 min. The resulting supernatant (S2) was collected. The pellet (P1) was resuspended in buffer A and centrifuged at 11,000×*g* for 30 min; supernatant (S3) was collected. Both S2 and S3 supernatants were divided equally and each fraction was incubated with 500 μL photoaffinity or control reagent conjugated to Neutravidin beads for 75 min at 4°C with shaking. The beads were collected by centrifugation then resuspended in buffer A + 1% (v/v) Triton X-100 and irradiated with 365 nm UV light (Mercury bulb H44GS100 from

Sylvania in a Blak-Ray 100A long-wave UV lamp with output of 25 mW/cm^2 at sample distance) for 30 min at 4°C. The beads were then washed in high-salt buffer containing 25 mM Tris-HCl pH 7.4, 350 mM NaCl, 1% (v/v) Triton X-100 and 1 mM PMSF. The beads were washed again in salt-free buffer containing 25 mM Tris-HCl, 1% (v/v) Triton X-100 and 1 mM PMSF. After 5 min incubation, the beads were collected, then boiled in SDS-PAGE gel loading dye containing 2-mercaptoethanol for 10 min at 70°C to release the bound proteins. After boiling, the contents were allowed to cool and after a quick spin the eluate was collected using a Hamilton syringe. The eluates were then analyzed in 4–20% (w/v) gradient SDS-PAGE and the protein bands were visualized using silver staining.[2] The protein bands pulled down specifically by photo-affinity reagent were excised from the silver stained SDS-PAGE gel and analyzed by mass spectrometry (IUSM Proteomics Core). Using Sequest™ algorithms and the swine database (UniProt), the identities of the pulled down proteins were confirmed (Supplementary Figure 1).

Immunoblot Assay. Cell lysates were prepared by homogenizing retina and choroid in NP-40 lysis buffer (25 mM HEPES pH 7.6, 150 mM NaCl, 1% (v/v) NP-40, 10% (v/v) glycerol, 1 mM sodium orthovanadate, 10 mM NaF, 1 mM PMSF, 10 μg/mL aprotinin, 1 μM pepstatin, 1 μM leupeptin) and then centrifuged at 12,000×*g* for 15 min at 4°C. Supernatant was collected and protein concentration was determined using a Bradford assay. Equal amounts of total protein (40 μg) from each sample were resolved by 10% (w/v) SDS-PAGE and then transferred onto PVDF membranes. Proteins were immunoblotted with antibodies against sEH (H215) (Santa Cruz) at 1:1000 dilution, and

β-actin (AC40) (Sigma-Aldrich) at 1:5000. Secondary antibodies (Thermo Fisher Scientific) were used at 1:10,000 dilutions. All of the dilutions were made in Tris Buffered Saline-0.05% (v/v) Tween-20 buffer containing 2% (w/v) bovine serum albumin (BSA). Signals were detected using Amersham ECL immunoblotting detection reagents on a Typhoon molecular imager (GE Healthcare).

Protein Structure Preparation for Molecular Dynamics. A crystal structure of sEH (PDB ID: 3I28[3]) was retrieved and prepared using the Protein Preparation Wizard in the Schrödinger software package (Schrödinger LLC).[4, 5] Bond orders were assigned and hydrogen atoms were added. Missing side chains and loops were introduced using the Prime module.[6] The resulting protein structure was protonated at pH 7.0 using PROPKA.[7]

Ligand Preparation for Docking. Compound SH-11037 was prepared using LigPrep.[4] Epik was used for protonation-state assignment and tautomer generation.[8] The OPLS_2005 force field was used for minimization and ionization states were generated at pH 7.[9] Compound was desalted to exclude additional molecules such as counter ions in salt and water molecules and tautomers were generated. All possible stereoisomer states were generated for a given compound, up to 32 different states per ligand.

Docking. Molecular docking was performed by Glide in standard-precision (SP) model.[10-12] The grids for docking were generated using the receptor grid generation tool in Maestro using an inner box of size 14 Å ×14 Å ×14 Å with dock ligands less than or

equal to 21 Å, and other settings left at the default. The docking mode of benzene ring exposed was selected for the final structure, as the *para* position of the benzene provides the probability of attachment of the linker.

Molecular Dynamics Simulations. The final docking model was used to run molecular dynamics simulations using the AMBER14 software package.[13] The compound was assigned AM1-BCC[14] charges and gaff[15] atom types using *antechamber*.[16] Crystal water molecules were retained. Complexes were immersed in a box of TIP3P water molecules.[17] No atom on the complex was within 14 Å from any side of the box. The solvated box was further neutralized with Na^+ or Cl^- counterions using the *tleap* program. Simulations were carried out using the GPU accelerated version of the *pmemd* program with ff14SB[18] and gaff force fields[15] in periodic boundary conditions. All bonds involving hydrogen atoms were constrained by using the SHAKE algorithm[19], and a 2 femtosecond (fs) time step was used in the simulation. The particle mesh Ewald (PME) method[20] was used to treat long-range electrostatics. Simulations were run at 298 K under 1 atm in NPT ensemble employing Langevin thermostat and Berendsen barostat. Water molecules were first energy-minimized and equilibrated by running a short simulation with the complex fixed using Cartesian restraints. This was followed by a series of energy minimizations in which the Cartesian restraints were gradually relaxed from 500 kcal·$Å^{-2}$ to 0 kcal·$Å^{-2}$, and the system was subsequently gradually heated to 298 K with a 48 ps molecular dynamics run. For each complex, we generated 10 independent simulations (replicates) that are each 10 ns in length. The initial velocity

of each replicate was randomly assigned. In total, 100 ns of simulation was run for each complex.

MMGBSA Free Energy Calculations. In the 10 trajectories (10 ns in length), the first 2 ns were discarded for equilibration. Snapshots were saved every 1 ps, yielding 8000 structures per trajectory. A total of 80000 snapshots were generated in 100 ns of simulation. 1000 snapshots were selected at regular intervals from the 80000 snapshots for free energy calculations using the *cpptraj* program.[21] The Molecular Mechanics-Generalized Born Surface Area (MM-GBSA)[22] method was used to calculate the free energy using the *MMPBSA.py* script.[23] The calculation using the GB method was performed with *sander* and Onufriev's GB model.[24, 25] Solvent-accessible surface area (SASA) calculations were switched to the icosahedron (ICOSA) method, where surface areas are computed by recursively approximating a sphere around an atom, starting from an icosahedron. Salt concentration was set to 0.1 M. The entropy was determined by normal mode calculations [26] with the *mmpbsa_py_nabnmode* module by selecting 50 of the 1000 snapshots used in the free energy calculations at regular intervals. The maximum number of cycles of minimization was set to 10000. The convergence criterion for the energy gradient to stop minimization was 0.5. In total, 1000 frames were used for each MM-GBSA calculation while 50 frames were used for each normal mode analysis. All other parameters were left at default values.

The MM-GBSA binding free energy is expressed as:

$$\Delta G_{\text{MM-GBSA}} = \Delta E_{\text{GBTOT}} - T\Delta S_{\text{NMODE}}$$

where ΔE_{GBTOT} is the combined internal and solvation energies, T is the temperature (298.15 K), and ΔS_{NMODE} is the entropy determined by normal mode calculations. The total enthalpy from the generalized Born model, ΔE_{GBTOT}, is the sum of 4 components:

$$\Delta E_{GBTOT} = \Delta E_{VDW} + \Delta E_{ELE} + \Delta E_{GB} + \Delta E_{SURF}$$

where ΔE_{VDW} and ΔE_{ELE} are the van der Waals and electrostatic energies, respectively, and ΔE_{GB} and ΔE_{SURF} are the polar and non-polar desolvation energies, respectively. All binding energies are determined by:

$$\Delta E = E^{COM} - E^{REC} - E^{LIG}$$

where E^{COM}, E^{REC} and E^{LIG} are total energies corresponding to the complex, receptor, and ligand, respectively.

Recombinant Soluble Epoxide Hydrolase Activity Assay. Small molecule inhibition of soluble epoxide hydrolase (sEH) enzymatic activity was evaluated using the sEH inhibitor screening assay kit based on the synthetic, fluorogenic substrate PHOME (3-phenyl-cyano(6-methoxy-2-naphthalenyl)methyl ester-2-oxiraneacetic acid) (Cayman Chemical) following manufacturer's instructions, using varying concentrations of SH-11037 (**1**) (synthesized as described[27]), *t*-AUCB (**5**) (Cayman Chemical), and **6** (synthesized as described[27]). Benzisoxazole sEH inhibitor **7** was synthesized according to a published method, and characterization matched published parameters.[28] Purity of all synthesized compounds was >95% by HPLC. Compounds were dissolved in DMSO (final DMSO concentration = 5% (v/v)). Activity was calculated according to:

$$\% \text{ Initial Activity} = [(F_{I15} - F_{I0})/(F_{T15} - F_{T0})] \times 100\%$$

Where F_I is the background corrected fluorescence signal obtained in the presence of an inhibitor and F_T is the background corrected fluorescence signal obtained for the total activity at times 0 and 15 minutes. IC_{50} values were calculated using GraphPad Prism v. 7.0.

sEH Enzyme Kinetics. Various concentrations of compound dissolved in DMSO (final DMSO concentration = 5% (v/v)) and human sEH (60 ng/mL final concentration; Cayman Chemical) in 25 mM bis-Tris-HCl buffer containing 0.1% (w/v) BSA were mixed in a 96 well plate. PHOME at indicated concentrations was added to the wells to initiate the reaction and fluorescence was read with an excitation wavelength of 330 nm and emission wavelength of 465 nm. The standard curve plotted from dilutions of the product, 6-methoxy-2-naphthaldehyde, was used to convert fluorescence reading (RFU/min) to sEH activity (nmol product formed/min). The reaction rate was obtained from the slope of the line from time = 5 to 15 minutes for each substrate concentration, and analyzed using GraphPad Prism 7 and SigmaPlot 13.0 to determine Michaelis-Menten kinetic parameters.

Mice. All mouse experiments followed the guidelines of the Association for Research in Vision and Ophthalmology Statement for the Use of Animals in Ophthalmic and Visual Research and were approved by the Indiana University School of Medicine Institutional Animal Care and Use Committee. Wild-type female C57BL/6J mice, 6–8 weeks of age, were purchased from the Jackson Laboratory. Intraperitoneal injections of 17.5 mg/kg ketamine hydrochloride and 2.5 mg/kg xylazine mixture were used for anesthesia. At

the end of the experiments, mice were euthanized by carbon dioxide asphyxiation followed by cervical dislocation.

Laser-induced Choroidal Neovascularization. The L-CNV mouse model and injections were performed as previously described.[29] Briefly, eyes were dilated using 1% (w/v) tropicamide, then underwent laser treatment using 50 μm spot size, 50 ms duration, and 250 mW pulses of an ophthalmic argon green laser, wavelength 532 nm, coupled to a slit lamp. Compounds where indicated were injected a single time immediately post-laser treatment, delivered intravitreally using a 33-gauge needle, in a 0.5 μL volume. SH-11037, *t*-AUCB, or **7** were dissolved in DMSO then diluted in PBS to a final concentration of 0.5% (v/v) DMSO. Vehicle alone (PBS + 0.5% (v/v) DMSO) was used as negative control. Mouse anti-$VEGF_{164}$ antibody (AF-493-NA, R&D Systems) at a 5 ng dose was used as a positive control for inhibition of neovascularization. Eyes were numbed with tetracaine solution before the injection, and triple antibiotic ointment was used immediately after the injection to prevent infection.

Lipid Profiling. C57BL/6J mice underwent laser treatment followed by intravitreal injections of 10 μM SH-11037, 10 μM *t*-AUCB or vehicle control as described above. Mice were sacrificed 3 days post-laser-treatment, eyes were enucleated and retina/choroid layers were immediately separated and stored at –80°C. Lipid profile analysis was performed by the Lipidomics Core Facility at Wayne State University using standard operating procedures developed by the core as previously described.[30]

Immunohistochemistry. Eyes from L-CNV and control mice fixed in 4% (w/v) PFA overnight were paraffin embedded and sectioned. Human donor eyes from wet AMD patients or age-matched controls with no documented ocular pathology were obtained from the National Disease Research Interchange (NDRI; Philadelphia, PA) with full ethical approval for use in research. All sample tissues were anonymized prior to receipt in the laboratory. Eye sections were deparaffinized, rehydrated and underwent heat induced antigen retrieval. Sections were washed in TBS and blocked in 10% (v/v) DAKO diluent in TBST/1% (w/v) BSA for an hour at room temperature, then incubated with primary antibodies overnight at 4°C. Primary antibodies and dilutions used were rabbit anti-sEH, H215 (1:250 for mouse, 1:90 for human; Santa Cruz); mouse anti-sEH, A5 (1:250; Santa Cruz); *Ricinus communis* agglutinin I (rhodamine labeled, 1:250 for mouse; FITC-labeled, 1:400 for human; Vector Labs); mouse anti-rhodopsin, ab3424 (1:300; Abcam); rabbit anti-cone arrestin, AB15282 (1:500; Millipore); mouse-anti-calbindin, ab11426 (1:300, Abcam); rabbit anti-Brn3a, AB5945 (1:400; Millipore); and rabbit anti-vimentin PLA0199 (1:300; Sigma) diluted in 10% (v/v) DAKO diluent in TBST/1% (w/v) BSA (only PBS/1% (w/v) BSA for human). Sections were then incubated with secondary antibodies, Alexa Fluor 488 (647 for human) goat anti-rabbit and Alexa Fluor 555 goat anti-mouse (Abcam) diluted 1:400 (1:500 for human) in 10% (v/v) DAKO diluent in TBST/1% (w/v) BSA (only PBS/1% (w/v) BSA for human) for 45–60 minutes at room temperature, followed by a brief wash in TBS, dehydration through an ethanol series and mounting with Vectashield mounting medium with DAPI (Vector Labs). Images were acquired with an LSM700 confocal microscope (Zeiss) with a 20x objective or, for human sections, an AxioImager D2 (Zeiss).

Tissue-based sEH Activity Assay using *trans*-Stilbene Oxide. The sEH activity in tissue homogenates was assayed using *trans*-stilbene oxide (*t*-SO) as substrate. The assay is based on the hydrolysis of *t*-SO that is tracked as a decrease in the absorbance at 230 nm.[31, 32] L-CNV was induced as described above. After 3 days, enucleated eyes from both untreated and L-CNV mice were homogenized in 0.2 M sodium phosphate buffer, pH 7.4. In order to remove microsomal epoxide hydrolase and lenses, tissue extracts were centrifuged at 100,000×*g* for 30 minutes at 4°C. After protein estimation, 100 μL of tissue homogenates (100 μg/mL) and 98 μL of SH-11037 or **7** dissolved in DMSO/buffer (final 1% (v/v) DMSO) were added to a UV-transparent 96-well plate. After 5 minutes' incubation at room temperature, 2 μL of *t*-SO in ethanol (100 μM final concentration) was added to assay wells to initiate the reaction. The absorbance was read at 230 nm for 20 minutes. sEH activity was determined as follows:

$$\text{sEH Activity} = [(A_0 - A_{20}) - (B_0 - B_{20})]/\text{mg of protein in a reaction}$$

Where A_0 and A_{20} are absorbance of test wells read at 230 nm at time 0 and 20 minutes respectively, and B_0 and B_{20} are absorbance of background wells read at 230nm at time 0 and 20 minutes.

Choroidal Flatmount and Analysis. To assess neovascularization in response to treatments, 14 days post-L-CNV induction, eyes were enucleated, fixed and stained as described.[33] Choroid/sclera layers were incubated with rhodamine labeled *Ricinus communis* agglutinin I (Vector Labs), in the dark for 45 minutes, to stain blood vessels. Flatmounts of the choroid were mounted with Vectashield mounting medium (Vector

Labs) and *Z*-stack images were taken on an LSM700 confocal microscope (Zeiss). ImageJ software was used to analyze *Z*-stack images. This experiment was performed by a masked investigator and followed the guidelines and exclusion criteria described previously,[34] to ensure reproducibility and eliminate investigator bias.

Choroidal Sprouting Assay. Sprouting of endothelial cells from choroidal layers was tested as previously described.[33] *t*-AUCB or **7** dissolved in DMSO was tested at 0.1, 1, and 10 μM concentrations for 48 hours. The final concentration of DMSO in each well was 0.2% (v/v). Images were taken using an EVOS-fl digital microscope (AMG) and data were analyzed as the sprouting distance in four different directions using ImageJ software v.1.48v (http://imagej.nih.gov/ij/).

Statistical Analyses. Statistical analyses were performed with GraphPad Prism 7 software. One-way ANOVA was used with Tukey's post hoc test for lipid profiling and sEH analysis in tissue, and Dunnett's post hoc test for L-CNV confocal analysis and choroidal sprouting experiments. Two-sided *P* values < 0.05 were considered statistically significant.

SUPPLEMENTARY REFERENCES

1. Lee, B., Sun, W., Lee, H., Basavarajappa, H., Sulaiman, R. S., Sishtla, K., Fei, X., Corson, T. W., and Seo, S. Y. (2016) Design, synthesis and biological evaluation of photoaffinity probes of antiangiogenic homoisoflavonoids, *Bioorg. Med. Chem. Lett. 26*, 4277–4281.

2. Corson, T. W., Cavga, H., Aberle, N., and Crews, C. M. (2011) Triptolide directly inhibits dCTP pyrophosphatase, *ChemBioChem 12*, 1767–1773.

3. Eldrup, A. B., Soleymanzadeh, F., Taylor, S. J., Muegge, I., Farrow, N. A., Joseph, D., McKellop, K., Man, C. C., Kukulka, A., and De Lombaert, S. (2009) Structure-based optimization of arylamides as inhibitors of soluble epoxide hydrolase, *J. Med. Chem. 52*, 5880–5895.

4. Sastry, G. M., Adzhigirey, M., Day, T., Annabhimoju, R., and Sherman, W. (2013) Protein and ligand preparation: parameters, protocols, and influence on virtual screening enrichments, *J. Comput.-Aided Mol. Des. 27*, 221–234.

5. Greenwood, J. R., Calkins, D., Sullivan, A. P., and Shelley, J. C. (2010) Towards the comprehensive, rapid, and accurate prediction of the favorable tautomeric states of drug-like molecules in aqueous solution, *J. Comput.-Aided Mol. Des. 24*, 591–604.

6. Jacobson, M. P., Pincus, D. L., Rapp, C. S., Day, T. J., Honig, B., Shaw, D. E., and Friesner, R. A. (2004) A hierarchical approach to all-atom protein loop prediction, *Proteins 55*, 351–367.

7. Olsson, M. H., Sondergaard, C. R., Rostkowski, M., and Jensen, J. H. (2011) PROPKA3: Consistent treatment of internal and surface residues in empirical pK_a predictions, *J. Chem. Theory Comput. 7*, 525–537.

8. Shelley, J. C., Cholleti, A., Frye, L. L., Greenwood, J. R., Timlin, M. R., and Uchimaya, M. (2007) Epik: a software program for pK_a prediction and protonation state generation for drug-like molecules, *J. Comput.-Aided Mol. Des. 21*, 681–691.

9. Banks, J. L., Beard, H. S., Cao, Y., Cho, A. E., Damm, W., Farid, R., Felts, A. K., Halgren, T. A., Mainz, D. T., Maple, J. R., Murphy, R., Philipp, D. M., Repasky, M. P., Zhang, L. Y., Berne, B. J., Friesner, R. A., Gallicchio, E., and Levy, R. M. (2005) Integrated Modeling Program, Applied Chemical Theory (IMPACT), *J. Comput. Chem. 26*, 1752–1780.

10. Friesner, R. A., Murphy, R. B., Repasky, M. P., Frye, L. L., Greenwood, J. R., Halgren, T. A., Sanschagrin, P. C., and Mainz, D. T. (2006) Extra precision glide: docking and scoring incorporating a model of hydrophobic enclosure for protein-ligand complexes, *J. Med. Chem. 49*, 6177–6196.

11. Halgren, T. A., Murphy, R. B., Friesner, R. A., Beard, H. S., Frye, L. L., Pollard, W. T., and Banks, J. L. (2004) Glide: a new approach for rapid, accurate docking and scoring. 2. Enrichment factors in database screening, *J. Med. Chem. 47*, 1750–1759.

12. Friesner, R. A., Banks, J. L., Murphy, R. B., Halgren, T. A., Klicic, J. J., Mainz, D. T., Repasky, M. P., Knoll, E. H., Shelley, M., Perry, J. K., Shaw, D. E., Francis, P., and Shenkin, P. S. (2004) Glide: a new approach for rapid, accurate docking and scoring. 1. Method and assessment of docking accuracy, *J. Med. Chem. 47*, 1739–1749.

13. Case, D. A., Berryman, J. T., Betz, R. M., Cerutti, D. S., T.E. Cheatham, I., Darden, T. A., Duke, R. E., Giese, T. J., Gohlke, H., Goetz, A. W., Homeyer, N., Izadi, S., Janowski, P., Kaus, J., Kovalenko, A., Lee, T. S., LeGrand, S., Li, P., Luchko, T., Luo, R., Madej, B., Merz, K. M., Monard, G., Needham, P., Nguyen, H., Nguyen, H. T., Omelyan, I., Onufriev, A., Roe, D. R., Roitberg, A., Salomon-Ferrer, R., Simmerling, C. L., Smith, W., Swails, J., Walker, R. C., Wang, J., Wolf, R. M., Wu, X., York, D. M., and Kollman, P. A. (2015) AMBER 2015, University of California, San Francisco.

14. Jakalian, A., Jack, D. B., and Bayly, C. I. (2002) Fast, efficient generation of high-quality atomic charges. AM1-BCC model: II. parameterization and validation, *J. Comput. Chem. 23*, 1623–1641.

15. Wang, J., Wolf, R. M., Caldwell, J. W., Kollman, P. A., and Case, D. A. (2004) Development and testing of a general amber force field, *J. Comput. Chem. 25*, 1157–1174.

16. Wang, J., Wang, W., Kollman, P. A., and Case, D. A. (2006) Automatic atom type and bond type perception in molecular mechanical calculations, *J. Mol. Graphics Modell. 25*, 247–260.

17. Jorgensen, W. L., Chandrasekhar, J., Madura, J. D., Impey, R. W., and Klein, M. L. (1983) Comparison of simple potential functions for simulating liquid water, *J. Chem. Phys. 79*, 926–935.

18. Maier, J. A., Martinez, C., Kasavajhala, K., Wickstrom, L., Hauser, K. E., and Simmerling, C. (2015) ff14SB: Improving the accuracy of protein side chain and backbone parameters from ff99SB, *J. Chem. Theory Comput. 11*, 3696–3713.

19. Ryckaert, J. P., Ciccotti, G., and Berendsen, J. J. C. (1977) Numerical integration of the cartesian equations of motion of a system with constraints: Molecular dynamics of n-alkanes, *J. Comput. Phys. 23*, 327–341.

20. Darden, T., York, D., and Pedersen, L. (1993) Particle mesh Ewald: An N·log(N) method for Ewald sums in large systems, *J. Chem. Phys. 98*, 10089–10092.

21. Roe, D. R., and Cheatham, T. E., 3rd. (2013) PTRAJ and CPPTRAJ: Software for processing and analysis of molecular dynamics trajectory data, *J. Chem. Theory Comput. 9*, 3084–3095.

22. Still, W. C., Tempczyk, A., Hawley, R. C., and Hendrickson, T. (1990) Semianalytical treatment of solvation for molecular mechanics and dynamics, *J. Am. Chem. Soc. 112*, 6127–6129.

23. Miller, B. R., 3rd, McGee, T. D., Jr., Swails, J. M., Homeyer, N., Gohlke, H., and Roitberg, A. E. (2012) MMPBSA.py: An efficient program for end-state free energy calculations, *J. Chem. Theory Comput. 8*, 3314–3321.

24. Onufriev, A., Bashford, D., and Case, D. A. (2004) Exploring protein native states and large-scale conformational changes with a modified generalized born model, *Proteins 55*, 383–394.

25. Feig, M., Onufriev, A., Lee, M. S., Im, W., Case, D. A., and Brooks, C. L., 3rd. (2004) Performance comparison of generalized born and Poisson methods in the calculation of electrostatic solvation energies for protein structures, *J. Comput. Chem. 25*, 265–284.

26. Brooks, B., and Karplus, M. (1983) Harmonic dynamics of proteins: normal modes and fluctuations in bovine pancreatic trypsin inhibitor, *Proc. Natl. Acad. Sci. U. S. A. 80*, 6571–6575.

27. Basavarajappa, H. D., Lee, B., Lee, H., Sulaiman, R. S., An, H., Magana, C., Shadmand, M., Vayl, A., Rajashekhar, G., Kim, E. Y., Suh, Y. G., Lee, K., Seo, S. Y., and Corson, T. W. (2015) Synthesis and biological evaluation of novel homoisoflavonoids for retinal neovascularization, *J. Med. Chem. 58*, 5015–5027.

28. Shen, H. C., Ding, F. X., Deng, Q., Xu, S., Tong, X., Zhang, X., Chen, Y., Zhou, G., Pai, L. Y., Alonso-Galicia, M., Roy, S., Zhang, B., Tata, J. R., Berger, J. P., and Colletti, S. L. (2009) A strategy of employing aminoheterocycles as amide mimics to identify novel, potent and bioavailable soluble epoxide hydrolase inhibitors, *Bioorg. Med. Chem. Lett. 19*, 5716–5721.

29. Sulaiman, R. S., Quigley, J., Qi, X., O'Hare, M. N., Grant, M. B., Boulton, M. E., and Corson, T. W. (2015) A simple optical coherence tomography quantification method for choroidal neovascularization, *J. Ocul. Pharmacol. Ther. 31*, 447–454.

30. Maddipati, K. R., and Zhou, S. L. (2011) Stability and analysis of eicosanoids and docosanoids in tissue culture media, *Prostaglandins Other Lipid Mediators 94*, 59–72.

31. Hasegawa, L. S., and Hammock, B. D. (1982) Spectrophotometric assay for mammalian cytosolic epoxide hydrolase using *trans*-stilbene oxide as the substrate, *Biochem. Pharmacol. 31*, 1979–1984.

32. Charles, R. L., Burgoyne, J. R., Mayr, M., Weldon, S. M., Hubner, N., Dong, H., Morisseau, C., Hammock, B. D., Landar, A., and Eaton, P. (2011) Redox regulation of soluble epoxide hydrolase by 15-deoxy-delta-prostaglandin J2 controls coronary hypoxic vasodilation, *Circ. Res. 108*, 324–334.

33. Sulaiman, R. S., Merrigan, S., Quigley, J., Qi, X., Lee, B., Boulton, M. E., Kennedy, B., Seo, S. Y., and Corson, T. W. (2016) A novel small molecule ameliorates ocular neovascularisation and synergises with anti-VEGF therapy, *Sci. Rep. 6*, 25509.

34. Poor, S. H., Qiu, Y., Fassbender, E. S., Shen, S., Woolfenden, A., Delpero, A., Kim, Y., Buchanan, N., Gebuhr, T. C., Hanks, S. M., Meredith, E. L., Jaffee, B. D., and Dryja, T. P. (2014) Reliability of the mouse model of choroidal neovascularization induced by laser photocoagulation, *Invest. Ophthalmol. Visual Sci. 55*, 6525–6534.